

# Learning Confident Classifiers in the Presence of Label Noise

Asma Ahmed Hashmi  
 Institute of Informatics, LMU Munich  
 Konrad Zuse School of Excellence in Reliable AI  
 asmah17@gmail.com

Aigerim Zhumabayeva  
 MBZUAI  
 Abu Dhabi, UAE  
 Aigerim.Zhumabayeva@mbzuai.ac.ae

Nikita Kotelevskii  
 Skoltech, MBZUAI  
 Russia, UAE  
 Nikita.Kotelevskii@skoltech.ru

Artem Agafonov  
 MBZUAI  
 Abu Dhabi, UAE  
 Artem.Agafonov@mbzuai.ac.ae

Mohammad Yaqub  
 MBZUAI  
 Abu Dhabi, UAE  
 mohammad.yaqub@mbzuai.ac.ae

Maxim Panov  
 MBZUAI  
 Abu Dhabi, UAE  
 Maxim.Panov@mbzuai.ac.ae

Martin Takáč  
 MBZUAI  
 Abu Dhabi, UAE  
 Takac.MT@gmail.com

## Abstract

*The success of Deep Neural Network (DNN) models significantly depends on the quality of provided annotations. In medical image segmentation, for example, having multiple expert annotations for each data point is common to minimize subjective annotation bias. Then, the goal of estimation is to filter out the label noise and recover the ground-truth masks, which are not explicitly given. This paper proposes a probabilistic model for noisy observations that allows us to build a confident classification and segmentation models. To accomplish it, we explicitly model label noise and introduce a new information-based regularization that pushes the network to recover the ground-truth labels. In addition, for segmentation task we adjust the loss function by prioritizing learning in high-confidence regions where all the annotators agree on labeling. We evaluate the proposed method on a series of classification tasks such as noisy versions of MNIST, CIFAR-10, Fashion-MNIST datasets as well as CIFAR-10N, which is real-world dataset with noisy human annotations. Additionally, for segmentation task, we consider several medical imaging datasets, such as, LIDC and RIGA that reflect real-world inter-variability among multiple annotators. Our experiments show that our algorithm outperforms state-of-the-art solutions for the considered classification and segmentation problems.*

## 1. Introduction

Real world data are replete with noisy labels. Since the labeling process of large-scale datasets is costly and time-consuming, researchers often resort to less expensive options, such as internet inquiries and crowdsourcing to circumvent this issue [45, 53]. Unfortunately, these methods are viable in producing datasets with incorrect labels. Smaller datasets are also vulnerable to the presence of corrupted labels. In this case, usually the labelling process is either challenging or the annotators have divergent opinions [4, 33]. In medical imaging, for example, it is imperative to procure annotations from the clinical experts. However, it is not only expensive to obtain annotated data, but it also suffers from high inter-reader variability among domain’s experts [26, 31], particularly in tasks such as segmentation and classification of images [21, 26]. Furthermore, the quality of the annotated labels became more intrinsic with the ubiquitous use of Deep Learning (DL) models in the medical domain [7, 42, 49], as the decision of the trainable models might have consequences for the health or even the life of a patient. Hence, developing DL algorithms that are robust to the noise in the annotated data is inarguably important.

DNNs noticeably suffer a degeneration in performance when trained on noisy labels. To combat this issue, various algorithms have been devised to adapt to the presence of noisy labels without compromising on the performance of DNNs. In classification, Sample Selection methods [14, 19, 34, 47, 55] started to gain momentum recently;

these methods involve a two networks approach, Student-Teacher, for learning from noisy labels. It uses a small loss trick to sample clean instances for additional training by its peer network. However, it does not perform well when the loss distribution of true-labelled and false-labelled examples overlap substantially.

In segmentation, and particularly in the medical imaging domain, while automated and semi-automated algorithms are being developed, manual segmentation remains the gold standard for the quantitative interpretation of medical images and validation of those semi- or fully-automated algorithms. However, manual delineation by radiologists or other experts often relies on their subjective interpretation that is augmented by their expertise.

The differences in annotations by multiple raters lead to inter-rater variability, which reflects the level of consistency between different raters in measuring the same target [21, 41]. This variability arises due to differences in experience, subject-specific expertise, and interpretation among the annotators. Moreover, the annotation task could be complex, time-consuming, and likely to be taxing; this inevitably leads to noise in the annotations, which degrades the model’s performance. To counter this, ground truth annotations are typically obtained through STAPLE [46] majority voting technique from multiple raters. This is done by selecting one preferred expert, or by using other label fusion approaches [3, 9, 17, 20, 23, 27, 32, 37, 57]. However, this process loses important agreement/disagreement information from all experts. In addition, while this technique is simple and easy to adopt, it comes at the expense of ignoring the underlying uncertainty information among various experts.

In this work, we aim to develop a new deep learning approach that achieves high-quality predictions in the presence of multiple annotators in the dataset. Inspired by [44, 56], our approach considers coupling two convolutional neural network architectures: a base classification network that estimates the true labels and an annotation network that estimates confusion matrices for each rater for a given input image. However, unlike other methods, we want to make a base network confident in predicting each class in the presence of the noisy labels alone. To accomplish it, we introduce the new regularization term that forces predictions to be close to the one-hot vector, with 1 being for the correct class and 0 for the rest. Such an approach assumes low ambiguity in ground truth annotations and attributes existing label uncertainty to the annotator’s noise. In addition, for segmentation tasks, we make use of the fact there are regions where all annotators agree and feed that information as input to the additional loss term that forces the confident predictions by the base segmentation network without the involvement of the annotation network.

**Contributions.** We summarize our contributions as fol-

lows.

1. We introduce a new “confidence” regularizer that allows to jointly learn the parameters of both base classification and annotation networks. It explicitly forces the model to learn confident predictions, thus allowing it to filter out the annotator noise in the problems with low ambiguity of ground truth labels.
2. For segmentation problem, we introduce a new term in the loss function, which takes into account the “agreement” between annotators in the regions where all of them give the same labels, thus forcing the direct application of the base segmentation model in the regions with a low annotation noise.
3. We provide a comprehensive set of experiments on MNIST, CIFAR-10, Fashion-MNIST and CIFAR-10N (real-world noisy data) datasets for classification. We also conducted a series of experiments on segmentation problems with annotation such as synthetic noisy data (based on MNIST) and real-world medical data (RIGA and LIDC). The experiments show that the proposed method provides state-of-the-art results in the considered problems.

Our `code` includes a suite that allows researchers to compare their approach against benchmarks considered in this paper.

## 2. Related Work

Learning with noisy labelled training data has been an active area of research for some time. Various algorithms have been introduced and have shown resistance to noise during training. We highlight the core research being done in this domain.

### 2.1. Classification

**Noise Transition Matrix/Loss Correction.** The loss correction approach [6, 10, 50] using a noise transition matrix,  $T$ , is a crucial branch that is used in deep learning systems. The goal of loss correction is for training on noisy labels with the corrected loss to be roughly equivalent to training on clean labels with the original loss.

Patrini et al. [38] introduced two different approaches for loss correction using a stochastic matrix  $T$  that delineates the probability of a class being flipped with another under a certain noise. To address extreme noise, Hendrycks et al. [15] suggested Gold Loss Correction (GLC) based on Forward Correction. Other similar works exploring this approach is [12, 39].

**Multi-Network Learning.** Multi-network [19, 34] training frequently employs collaborative learning and co-training. Therefore, the sample selection procedure is governed by the mentor network in the case of joint learning and the peer network in the case of co-training.

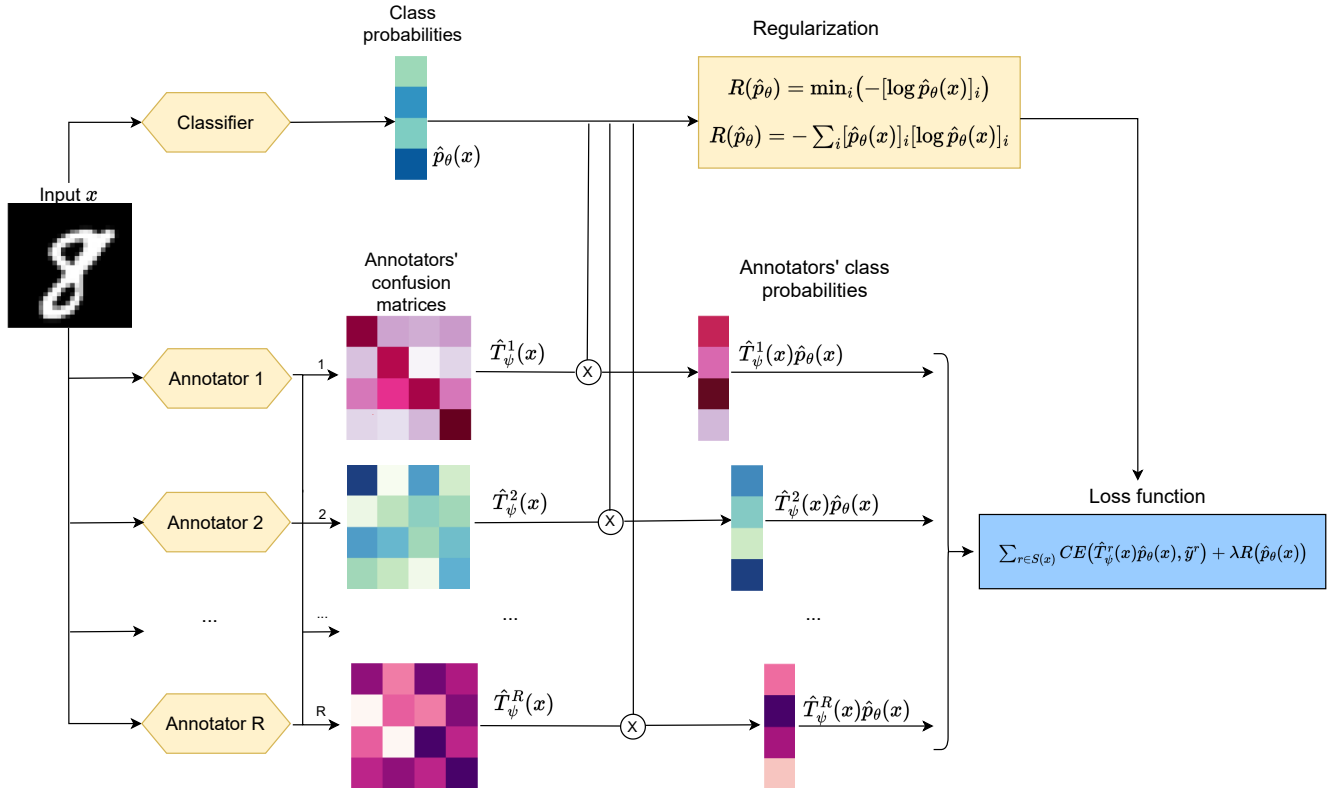


Figure 1. Illustration of the proposed architecture. The input image is fed into two separate networks – Base (in the particular case of this example – Classifier Network) and Annotation. Then, their predictions are multiplied to produce the prediction of the noisy (annotators) labels distribution. Finally, the loss function is computed, summing up all the components.

Co-teaching [14] and Co-teaching+ [55] also employ two DNNs, but each DNN selects a certain number of small-loss examples and feeds them to its peer DNN for additional training. In comparison, JoCoR [47] reduces the diversity of two networks by means of co-regularization, making the predictions of the two networks more similar.

**Robust Regularization.** Tanno et al. [44] showcased a method for simultaneously learning the individual annotator model and the underlying true label distribution through the use of trace regularization. Menon et al. [35] suggests a composite loss-based gradient clipping for label noise robustness, given that excessive trust is not placed in any single sample.

**Other Deep Learning/Statistical Methods.** Yi and Wu [54] proposed a framework that updates the label distributions through an iterative correction of the noisy labels. Xia et al. [51] suggested a robust early-training method to diminish the side effect of noisy labels prior to early stopping. DivideMix [28] splits the data into labelled (clean samples) and an unlabelled set (noisy samples) and train it in a semi-supervised approach.

## 2.2. Segmentation

Training deep neural networks on noisy label annotations can overfit to the noise in the dataset [43]. Inter-reader variability among annotators gave prominence to the Simultaneous Truth and Performance Level Estimation (STAPLE; [46]) algorithm that uses Expectation-Maximization to merge segmentation masks from various annotators into estimating a single ground truth. Several algorithms drew their inspiration from the STAPLE framework such as [3, 9, 17, 20, 23, 27, 32, 37, 57].

In [36], authors provide a sample re-weighting strategy that considers the expertise level of annotators. This strategy gives greater weights in the loss function for the samples annotated by professionals. To disengage annotator bias, Zhang et al. [56] uses two coupled CNNs. Similar to [44], the CNN for segmentation estimates the label distribution, while the CNN for annotation is representative of the annotator bias using a confusion matrix. Similar ideas were applied in [29], but with another regularization that led to the recovery of the ground truth confusion matrix and ground truth posterior  $p(y | x)$  under the assumption of diagonal dominance for the confusion matrix.

Recently, various projects have begun to investigate the impact of multi-rater labels using label sampling [16, 22] or multi-head [13] techniques. Models trained with multi-rater labels are believed to be better calibrated than those trained with traditional ground-truth labels, such as majority vote, which are prone to overconfidence [16, 22]. In another pivotal work in the domain, Kohl et al. [24] proposed to learn a distribution of probable segmentations from the given input image; it integrates a U-Net [40] and conditional Variational Autoencoders (VAE) to effectively develop an extensive number of conceivable hypothesis/segmentation results.

### 3. Methodology

#### 3.1. Noisy Labels in Deep Learning

In this section, we introduce the problem of training a deep learning model in the presence of multiple annotations. Since each of the annotations is received from some expert with his expertise and biases, we consider these annotations as “noisy”.

Let  $\mathcal{X}$  denote the space that contains a set of input training data  $X := \{x_1, \dots, x_N\}$ . Each of these objects  $x_i$  has a corresponding ground-truth label  $y_i$  such that  $Y := \{y_1, y_2, \dots, y_N\} \subseteq \mathcal{Y}$ , where  $\mathcal{Y}$  is the space of labels. However, in many scenarios, we don’t have access to ground-truth labels and only have potentially noisy annotations available. Thus, we assume our training dataset  $\mathcal{D}$  to be a collection of  $N$  input images  $x_i$  and their corresponding noisy annotations received from a subset of fixed annotators. By  $S(x_i)$ , we denote the set of indices of those annotators who provided their annotations for an input image  $x_i$ . We assume that overall we have  $R$  annotators, and their identities are preserved for all the images.

The dataset therefore has the following structure:  $\mathcal{D} = \{x_i, \{\tilde{y}_i^r\}_{r \in S(x_i)}\}_{i=1}^N$ , where  $\tilde{y}_i^r$  corresponds to an annotation of  $r$ -th expert for the input image  $x_i$ . The tilde sign reminds us that the annotation is noisy.

It is worth noting that the ground truth annotations  $y_i$  are not available to us but assumed to exist. Thus, our goal is to build a model which will approximate the distribution of targets  $p(y_i | x_i)$  for a given input solely from the dataset of noisy annotations.

#### 3.2. Probabilistic Model for Noisy Observations and Architecture

In this section, we build a probabilistic noise model for observed noisy annotations. Following [44, 56], we assume statistical independence of annotators.

For the following derivations, we will omit the object index  $i$  to simplify the notation. Taking these assumptions into account, we can write the joint likelihood for all anno-

tations  $\{\tilde{y}^r\}_{r \in S(x)}$  of a given input image  $x$ :

$$p(\{\tilde{y}^r\}_{r \in S(x)} | x) = \prod_{r \in S(x)} p(\tilde{y}^r | x). \quad (1)$$

Each of the probabilities  $p(\tilde{y}^r | x)$  inside the product is an implicit marginalization of the latent ground truth class label  $y$ :

$$p(\tilde{y}^r | x) = \sum_{c=1}^C p(y = c | x) p(\tilde{y}^r | y = c, x),$$

where  $C$  represents the number of classes for the true labels,  $y \in [1, \dots, C]$ .

Since the annotators’ noise is dependent on the sample  $x$ , this allows us to model noisy label distribution as  $p(\tilde{y}^r = j | y = i, x) =: u_{ji}^r(x)$ . These noisy class conditional distributions can be considered as elements of a confusion matrix (CM), effectively modeling the noise introduced by the annotator. We denote by  $U^r(x)$  a  $C \times C$  confusion matrix  $[U^r]_{j,i}(x) = u_{ji}^r(x)$ . Now, the marginalization can be rewritten as follows:

$$\begin{aligned} p(\tilde{y}^r | x) &= \sum_{c=1}^C p(y = c | x) p(\tilde{y}^r | y = c, x) \\ &= \sum_{c=1}^C u_{\tilde{y}^r c}^r(x) \cdot p(y = c | x). \end{aligned} \quad (2)$$

In this equation, we see that the predictive distribution for a noisy annotation is a mixture of class-conditional distributions of noisy annotations weighed by the ground truth label distributions.

Inspired by [44, 56], we use a two-component model to approximate the distributions in equation (2). The first component is the base prediction network, which solves the problem of interest. In the case of classification, we call it classification model, in the case of segmentation – segmentation model. The other component is an annotation network. The base prediction network is a convolutional neural network parameterized by  $\theta$  that aims to approximate the ground truth probability distribution  $p(y | x)$ . Hence, it transforms an input image  $x$  to a probability map  $\hat{p}_\theta(x) \in \mathbb{R}^C$  (for more details in the case of segmentation see Section A).

The annotation network, parameterized by  $\psi$ , provides an estimate of the CMs of the corresponding annotators as a function of the input image. Hence, this model, trained separately for each of the annotators, produces the matrix  $\hat{T}_\psi^r(x) \in [0, 1]^{C \times C}$ ,  $r \in S(x)$ . The element of this matrix, indexed by  $kl$ , equals to  $p(\tilde{y}^r = k | y = l, x)$ .

The multiplication of these two terms  $\hat{p}_{\theta, \psi}^r(x) = \hat{T}_\psi^r(x) \times \hat{p}_\theta(x)$  is the  $r$ -th annotator’s probability map which is optimized in the loss function (the details are covered in Section 4.1). The architecture of the resulting model for the case of classification is depicted in Figure 1.

## 4. Training and Confident Regularization

In this section, we explain in detail the training procedure we use and introduce a new regularizer specially tailored to the problems with label noise.

### 4.1. Loss function

We introduce a loss function, which allows us to jointly optimize the parameters  $\theta$  and  $\psi$  of the prediction and annotation networks.

For this, we maximize the likelihood of the observed noisy annotations. Using (2), we can rewrite the negative log-likelihood for  $N$  training objects in the following form:

$$\begin{aligned}
 & -\log \prod_{i=1}^N \prod_{r \in S(x_i)} \text{Cat}(\tilde{y}_i^r; p_{\psi, \theta}^r(x_i)) = \\
 & -\sum_{i=1}^N \sum_{r \in S(x_i)} \sum_{c=1}^C \mathbb{1}(\tilde{y}_i^r == c) \log p_{\psi, \theta}^r(x_i) = \\
 & \sum_{i=1}^N \sum_{r \in S(x_i)} CE(\hat{T}_{\psi}^r(x_i) \hat{p}_{\theta}(x_i), \tilde{y}_i^r), \quad (3)
 \end{aligned}$$

where  $CE$  stands for the cross-entropy and  $\text{Cat}$  stands for the probability mass function of Categorical distribution.

Minimizing the above objective function would jointly optimize both the parameters  $\theta$  and  $\psi$ . However, minimizing this function alone does not guarantee disentangling the annotator’s noise distribution from the ground truth label distribution. This is because there could be many combinations of  $\hat{T}_{\psi}^r(x) \hat{p}_{\theta}(x)$  that provide good approximations to  $\tilde{y}^r$ . This means that the prediction network’s output  $\hat{p}_{\theta}(x)$  may not learn to correctly discriminate between noise and true labels. To overcome this issue, one may consider introducing some regularizer  $R(\hat{p}_{\theta}(x))$  that would help the disentanglement.

Then, the resulting loss function parameterized by  $\lambda > 0$  becomes

$$\begin{aligned}
 \mathcal{L}(X, Y) = & \sum_{i=1}^N \sum_{r \in S(x_i)} CE(\hat{T}_{\psi}^r(x_i) \hat{p}_{\theta}(x_i), \tilde{y}_i^r) + \\
 & + \lambda \sum_{i=1}^N R(\hat{p}_{\theta}(x_i)). \quad (4)
 \end{aligned}$$

In the next section we will discuss the particular choice of the regularizer  $R(\hat{p}_{\theta}(x))$ .

### 4.2. Rationale for Confident Regularization

In this section, we discuss the choice of the regularizer needed for training the considered model. The motivation for using some regularizer is straightforward – there are infinitely many solutions for the components of the product  $\hat{T}_{\psi}^r(x) \hat{p}_{\theta}(x)$ , which maximizes the likelihood of noisy annotations.

Noise rate	Ours-Inf	Ours-Ent	Co-tea	Co-tea+	JoCoR	Trace	CDR
symmetric 20%	<b>84.22</b>	<u>84.00</u>	81.82	80.42	82.12	82.86	81.01
	$\pm 0.44$	$\pm 0.41$	$\pm 0.18$	$\pm 0.14$	$\pm 0.07$	$\pm 0.59$	$\pm 0.13$
symmetric 30%	<b>83.85</b>	<u>83.26</u>	80.69	79.64	80.95	80.45	78.90
	$\pm 0.68$	$\pm 0.64$	$\pm 0.20$	$\pm 0.13$	$\pm 0.10$	$\pm 0.70$	$\pm 0.54$
symmetric 50%	<b>80.03</b>	<u>79.64</u>	75.74	75.09	76.60	77.82	69.68
	$\pm 0.22$	$\pm 0.26$	$\pm 0.09$	$\pm 0.15$	$\pm 0.09$	$\pm 1.17$	$\pm 0.59$
symmetric 58%	<b>45.76</b>	<u>43.21</u>	19.84	18.01	28.32	33.61	35.38
	$\pm 0.11$	$\pm 0.15$	$\pm 0.10$	$\pm 0.08$	$\pm 0.35$	$\pm 1.21$	$\pm 0.40$
pairflip 20%	<b>84.92</b>	<u>84.78</u>	81.17	80.78	81.86	83.86	82.89
	$\pm 0.39$	$\pm 0.43$	$\pm 0.13$	$\pm 0.11$	$\pm 0.09$	$\pm 0.42$	$\pm 0.54$
pairflip 30%	<u>84.36</u>	<b>84.54</b>	79.53	79.49	79.52	83.15	82.08
	$\pm 0.43$	$\pm 0.39$	$\pm 0.16$	$\pm 0.12$	$\pm 0.25$	$\pm 0.46$	$\pm 1.33$
pairflip 45%	<b>83.43</b>	<u>81.23</u>	59.04	53.07	67.59	75.88	58.56
	$\pm 0.32$	$\pm 0.36$	$\pm 0.15$	$\pm 0.31$	$\pm 0.36$	$\pm 2.13$	$\pm 1.60$

Table 1. Comparison of test accuracy (%) (mean  $\pm$  st. dev.) for CIFAR-10. **Best** results are in bold, second-best underlined.

We start by discussing the regularizer from [44, 56]:

$$R_{tr}(x) = \text{trace} \left[ \frac{1}{|S(x)|} \sum_{r \in S(x)} \hat{T}_{\psi}^r(x) \right],$$

where  $\frac{1}{|S(x)|} \sum_{r \in S(x)} \hat{T}_{\psi}^r(x)$  is the confusion matrix averaged over annotators. The motivation of this regularizer is to push the estimated confusion matrix  $\hat{T}_{\psi}^r(x)$  to converge to the true confusion matrix of the annotator. It is shown in [56], that the minimizer of the trace includes true confusion matrix as a solution.

However, the proof present in [56] is based on some assumptions. Most importantly, they assume diagonal dominance of the mean confusion matrix  $\frac{1}{|S(x)|} \sum_{r \in S(x)} \hat{T}_{\psi}^r(x)$ . This assumption is not necessarily satisfied in practice. Moreover, the considered regularizer acts in the opposite direction, i.e., it pushes the estimate to be not diagonally dominant. Thus, this regularizer might only spoil the training process because, intuitively, it prevents annotators from being confident.

In this work, we propose a new regularizer that leads to better results without the need for regularizing parameters of the annotation network and the use of architecture modifications. Specifically, we push the base prediction network to provide confident predictions. Implicitly, we assume that there is no aleatoric noise in the ground-truth distribution of labels, the assumption previously considered in [56]. Hence,  $p(y | x) = \mathbf{e}$ , where  $\mathbf{e}$  is a one-hot vector with one placed to the correct label location. Based on these considerations, we introduce so-called *confidence* regularizer to the model’s loss function that penalizes the base prediction model for making uncertain predictions:

$$R(\hat{p}_{\theta}(x)) = \min_i (-\log \hat{p}_{\theta}(x)_i). \quad (5)$$

This function attains minimum if one of the predicted classes has predicted probability equal to 1.

Noise rate	Ours-Inf	Ours-Ent	Co-tea	Co-tea+	JoCoR	Trace	CDR
symmetric 20%	90.67	<u>90.79</u>	90.48	88.69	<b>91.88</b>	90.61	88.69
	$\pm 0.21$	$\pm 0.19$	$\pm 0.06$	$\pm 0.09$	$\pm 0.06$	$\pm 0.24$	$\pm 0.09$
symmetric 30%	<b>91.35</b>	90.34	90.36	88.50	<u>91.33</u>	89.64	87.38
	$\pm 0.25$	$\pm 0.26$	$\pm 0.13$	$\pm 0.09$	$\pm 0.08$	$\pm 0.30$	$\pm 0.09$
symmetric 50%	<b>89.51</b>	<u>89.49</u>	89.37	77.96	89.21	88.94	85.36
	$\pm 0.55$	$\pm 0.58$	$\pm 0.08$	$\pm 0.33$	$\pm 0.06$	$\pm 0.53$	$\pm 0.09$
pairflip 20%	<u>90.90</u>	90.77	90.68	89.12	<b>91.37</b>	90.40	90.01
	$\pm 0.33$	$\pm 0.29$	$\pm 0.05$	$\pm 0.08$	$\pm 0.09$	$\pm 0.35$	$\pm 0.11$
pairflip 30%	<u>90.38</u>	<b>90.65</b>	90.11	89.06	89.67	90.33	88.78
	$\pm 0.41$	$\pm 0.45$	$\pm 0.08$	$\pm 0.10$	$\pm 0.07$	$\pm 0.46$	$\pm 0.14$
pairflip 45%	<b>89.37</b>	89.02	78.86	52.61	88.10	<u>89.08</u>	64.63
	$\pm 0.68$	$\pm 0.71$	$\pm 0.11$	$\pm 0.43$	$\pm 0.39$	$\pm 0.72$	$\pm 0.17$

Table 2. Comparison of test accuracy (%) (mean  $\pm$  st.dev.) for Fashion-MNIST. **Best** results are in bold, second-best underlined.

Noise type	Ours-Ent	Co-tea	Co-tea+	JoCoR	Trace	CDR
worst	<b>73.58</b>	67.97	65.45	68.74	70.23	59.87
	$\pm 0.96$	$\pm 1.17$	$\pm 0.25$	$\pm 0.21$	$\pm 0.89$	$\pm 0.58$

Table 3. Comparison of test accuracy (%) (mean  $\pm$  st. dev.) for CIFAR-10N. **Best** results are in bold, second-best underlined.

## 5. Experiments

### 5.1. Classification

#### 5.1.1 Classification Task Baselines

We compare our algorithm with the following approaches

- Co-teaching [14], which simultaneously trains two DNN models, with each network selecting the batch of data for the other, based on the instances with a small loss.
- Co-teaching+ [55], also employs samples with small loss, but with disagreement about predictions. This is the selection criteria for the networks to pick data for each other.
- JoCoR [47], extends the idea of [14, 55] by using co-regularization to minimize the diversity of the two networks, thus bringing the predictions of the two networks closer together.
- Robust Early-learning (CDR; [51]), categorizes the critical and non-critical parameters for clean and noisy label fitting, respectively. Different update rules are applied to update these parameters.
- Annotator Confusion (Trace; [44]) is a regularized approach that assumes the existence of various annotators to simultaneously learn the individual annotator model and the underlying true label distribution, using only noisy observations.

#### 5.1.2 Datasets

In this work, we consider dataset with synthetically generated annotations along with annotations from human experts. For classification problem, we consider the standard benchmark datasets: MNIST [11], Fashion-MNIST [52], CIFAR-10 [25] where noises are generated synthetically and CIFAR-10N dataset (real world human annotations noisy data) [48] to demonstrate the effectiveness of our

methodology. The noise types, used in the classification experiments, are as follows.

- The pairflip noise involves swapping the labels of two adjacent categories/classes based on a preset ratio [30].
- The symmetric noise retains a portion of the original labels and uniformly reassigns the remainder to all other categories [33].
- The worst is the human label, which comprise of the highest amount of noise.

Detailed descriptions of datasets and examples of noise transition matrices are provided in Appendix B.2.

#### 5.1.3 Performance Evaluation

We conducted our experiments on four datasets that utilize artificial and real-world noisy labels. In our experiments for classification task, we synthetically introduced noise (pairflip and symmetric noise, see Section 5.2.3) to the training data for MNIST, Fashion-MNIST and CIFAR-10 dataset; we chose various noise rates, such as 20%, 30%, 45%, 50% and 80%. We used "worst" noise type for CIFAR-10N real world noisy annotations data; it comprised of 40% noise in the dataset. From these noisy labels, we are aimed to train a model which will be good at predicting ground-truth labels. Typically in deep learning, the best model is chosen based on the validation loss. However, to compute the loss for the model, we need to know ground-truth labels. Since in our case the true labels are unknown and we do not know when to stop, we run a significant amount of epochs. We evaluate the performance of our algorithm in terms of test accuracy for the classifier network as this aids in estimating the ground truth via making confident predictions about the true class. We are particularly interested in the performance of the classifier, as in evaluation stage this network will be used separately, to make predictions. Details on tuning the classification model can be found in Appendix C.3.

#### 5.1.4 Results

In this section, we present an extensive performance comparison analysis of our proposed approach with other methods for different datasets. The comparison analysis for each dataset is provided in separate Tables 1, 2, 3 and 10 (in Appendix C.3). For CIFAR-10, CIFAR-10N, and MNIST (Table 10 in Appendix C.3) datasets, our approaches yield the highest performance results across all noise rates and types. Our algorithm has shown robust performance across most baselines for Fashion-MNIST dataset. We see comparable performance among all the algorithms when the noise rate is 20% and 30% for both symmetric and pairflip noise types. In general, for higher noise ratios regardless of noise type, which are evidently more challenging cases, our algorithm consistently gives better performance as entropy and information regularization strategy helps the model to be more

Annotators	Original	Thin	Thick
Annotator 1	symmetric 80%	asymmetric 40%	pairflip 95%
Annotator 2	pairflip with permutation 40%	symmetric 95%	asymmetric 70%
Annotator 3	pairflip 60%	pairflip with permutation 40%	symmetric 80%

Table 4. Annotator information for three different styles (MNIST).

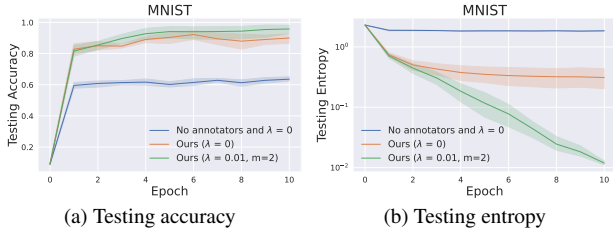


Figure 2. Accuracy and Entropy for Curated MNIST testing data on seven different seeds.

certain in its predictions. The results of our method with entropy and information-based regularizers are comparable.

**Curated Dataset.** We have assembled the dataset that is based on MNIST, where noise level depends on input image style for various annotators. Three types of image styles were simulated by performing morphological transformations (in particular, thinning and thickening) on the original images, using Morpho-MNIST software [8]. In addition to the noise types described in Section 5.2.3, asymmetric and pairflip with permutation were applied. The type and level of noises applied to original labels are provided in Table 4.

For a dataset consisting of three different types of images (original, thin, and thick) and three different annotators (Table 4), we compare (i) base classifier model without annotators and regularization, (ii) our approach without regularization, and (iii) our approach with information-based regularization. Each annotator NN has similar architecture as in classifier model and takes images as an input.

The result of experiments can be seen in Figures 2. Our approach is more accurate and confident compared to the classifier model. The accuracy of our approach with regularizer is higher and more confident than the model without the regularizer.

The proposed approach is able to learn the annotators’ confusion. Predicted confusion matrices for each annotator and different image types are provided in Figure 3. More results can be found in Appendix C.3.2.

## 5.2. Segmentation

### 5.2.1 Segmentation Task Baselines

We compare our approach with the following methods.

- CM-NET [56] uses two coupled CNN models that jointly estimate the true segmentation label distribution, as well as the reliability/confusion of the annotators from noisy labels. The strategy helps with disentangling human bias

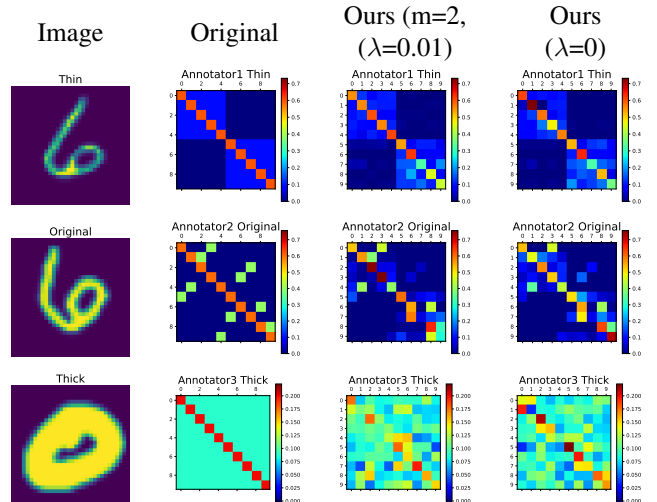


Figure 3. Original and Predicted confusion for different Annotators using different models: our approach with regularizer ( $\lambda = 0.01, m=2$ ) and without it ( $\lambda = 0$ ). (MNIST).

from the GT.

- PU-NET [24] incorporates a probabilistic model at each pixel in the output segmentation map. Instead of predicting a single label for each pixel, the network predicts a probability distribution over all possible labels.
- MR-NET [18] proposes a method that uses a deep learning model to learn from multiple annotations of the same image and generates a consensus segmentation that is calibrated to match the annotations.

We refer readers to the Appendix, Section C.2 for some additional experiments where we adapt the regularizer from [29] to segmentation problem and compare it to the approaches above.

### 5.2.2 “Confident regions” (CR) component in the loss

In this work, we also propose to directly apply the segmentation network  $\hat{p}_\theta(x_i)$  for predictions for the pixels with low labeling noise. We construct such confident regions (CR) by a special procedure. First, we find such areas of the annotation masks for which all the annotators assign the same label. Next, we use the heuristic that the pixels near the boundary of this region have a high potential for uncertainty. Because of this, we dilate the uncertainty region (complement of the unanimously segmented region) using the convolution operation with zero bias. The complement of this dilated uncertainty region is now a CR, which we will use in our loss function by adding a special term, see equation (4). The process of selecting the CR is illustrated by Figure 4.

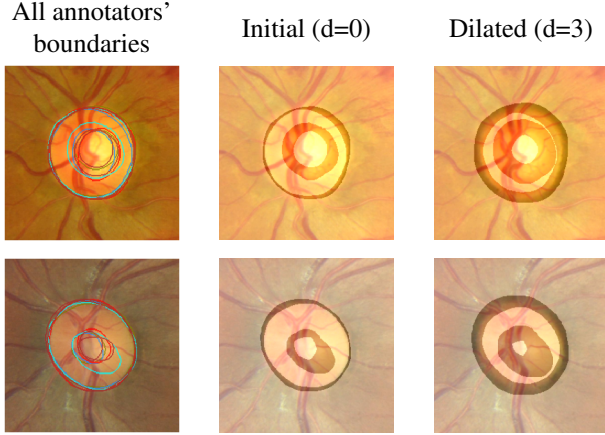


Figure 4. Visualization of CR with different dilation radius of uncertainty regions (RIGA Optical Cup). Here, uncertainty regions have natural colors, while CR is whitened.

### 5.2.3 Datasets

For segmentation problem we use MNIST [11] as a representative of dataset with artificial noises, where synthetic noisy annotations are created by applying morphological transformations simulations on assumed ground truth [8]. As an example of real world dataset we utilize retinal fundus images for glaucoma analysis (RIGA) [1] and the lung image database consortium (LIDC) [24] datasets. Detailed descriptions of datasets, examples of input and annotations are provided in Appendix B.1, Figures 6, 7, 8. Detailed descriptions of datasets and examples of samples are provided in Appendix B.2.

### 5.2.4 Performance Evaluation

We performed our experiments using three datasets with real-world and artificial noisy labels. To evaluate the segmentation model, use the Dice coefficient on validation splits and report its mean and standard deviation computed over the last 10 epochs. Note the Dice coefficients are calculated for each sample individually, and then the average value is taken. Although the Dice coefficient between the prediction  $\hat{p}_\theta(x)$  and true label  $y$  is more important, we also consider: Dice coefficient among the noisy annotations  $y_a$  ( $D(y_a, y_a)$ ), Dice coefficient among predictions of annotations ( $D(\tilde{y}_a, \tilde{y}_a)$ ), Dice coefficient between the annotations' predictions and noisy labels ( $D(\tilde{y}_a, y_a)$ ), Dice coefficient between noisy labels and true labels ( $D(y_a, y_{gt})$ ), and Dice coefficient between the annotations' predictions and true label ( $D(\tilde{y}_a, y_{gt})$ ). More details are provided in Appendix C.1. In the case of medical images, to make the evaluation, we compute the true label by majority voting. We emphasize that they are used only in the evaluation stage, not in the training. Along with these baseline models, we

Datasets	MR-Net	CM-Net	PU-NET	Ours (no conf)	Ours
MNIST	<u>95.81</u> $\pm 0.45$	93.85 $\pm 0.03$	89.90 $\pm 0.25$	94.47 $\pm 0.02$	<b>96.61</b> $\pm 0.00$
RIGA	<u>93.21</u> $\pm 1.12$	90.03 $\pm 0.91$	91.23 $\pm 1.21$	92.06 $\pm 0.58$	<b>93.85</b> $\pm 0.09$
LIDC	72.73 $\pm 2.70$	72.75 $\pm 0.66$	71.83 $\pm 1.50$	<u>75.93</u> $\pm 0.53$	<b>82.07</b> $\pm 0.92$

Table 5. Comparison of Dice coefficient (%) for different methods of segmentation task and datasets (mean  $\pm$  standard deviation). **Best results** are in bold, second-best underlined.

also run the model without involving the confidence region in our framework to see the effect of including it.

### 5.2.5 Segmentation Results

In this section, we present a quantitative analysis comparing the performance of our proposed method with various competing approaches across multiple datasets. In Table 5, we report the macro-averaged Dice coefficient, which is calculated as the average of individual class-wise scores. From this aggregate measure, it is seen that our method, enhanced with a confidence regions regularization, consistently outperforms the alternatives. Notably, the standard deviation observed for our approach is generally lower than those of our competitors, indicating the superior stability and reliability of our method.

Detailed tables for each dataset with all six types of Dice coefficients computed separately for each of the classes are provided in Appendix C.1 (Tables 6, 7, 8). It can be seen that our model with a confidence regularizer outperforms the competitors in terms of class-wise Dice coefficients for MNIST dataset. When applied to the LIDC dataset, our approach yields the highest performance with a substantial margin for class 1 (lungs) and second-best result for class 0 (background). Our models show robust performance for classes 0 (background) and 1 (optical disc) on RIGA dataset and achieve the highest score for class 2 (optical cup). In addition, to further illustrate these results, we have included additional visualizations of the final segmentations achieved on each dataset in the Appendix C.1, as depicted in Figures 11, 12, 13 and 14.

Additional experiments, which study the choice and effect of the regularizer, can be found in Appendix C.2.

## 6. Discussion

Our experimental results demonstrate that the proposed methodologies perform at least as effectively as competing approaches, frequently surpassing them in terms of both the average Dice coefficient (as shown in Table 5) and class-specific Dice scores for segmentation task and in terms of



test accuracy for classification task.

A notable observation that appears consistently across all datasets is the superior performance of our model when it uses the proposed confidence regularizer. Moreover, for segmentation, the regularized model shows consistently higher Dice scores than the model without regularization across all classes and datasets.

This consistency of the best performance, regardless of the diversity and complexity of datasets, shows the generalization capability of our model and proposed regularizers, which reassures its potential as a valuable tool for classification and image segmentation tasks of medical data.

## 7. Conclusion

In this paper, we have introduced a new approach for training classification model with noisy labels and segmentation model under the scenario of multiple noisy annotators. Our key contribution is the introduction of a regularizer which, unlike previous methods, exclusively penalizes the parameters of the base prediction network, thereby incentivizing the model to make more confident predictions. This regularizer allows to improve the results over the competing approaches.

Moreover, we introduce the concept of confident regions for the segmentation problem, identified as regions where all annotators unanimously agree on their predictions, into our loss function. This allows us to push the segmentation model explicitly to predict the class selected by all the annotators. We observed empirically that this consistently helps to improve the results.

## References

- [1] Ahmed Almazroa, Sami Alodhayb, Essam A Osman, Eslam Ramadan, Mohammed Hummadi, Mohammed Dlain, Muhammad Alkatee, Kaamran Raahemifar, and Vasudevan Lakshminarayanan. Agreement among ophthalmologists in marking the optic disc and optic cup in fundus images. *International Ophthalmology*, 37:701–717, 2017. 8, 3
- [2] Samuel G Armato III, Geoffrey McLennan, Luc Bidaut, Michael F McNitt-Gray, Charles R Meyer, Anthony P Reeves, Binsheng Zhao, Denise R Aberle, Claudia I Henschke, Eric A Hoffman, et al. The lung image database consortium (lidc) and image database resource initiative (idri): a completed reference database of lung nodules on ct scans. *Medical physics*, 38(2):915–931, 2011. 1
- [3] Landman BA Asman AJ. Robust statistical label fusion through consensus level, labeler accuracy, and truth estimation (collate). *IEEE transactions on medical imaging*, pages 1779–94, 2011. 2, 3
- [4] Ella Barkan, Alon Hazan, and Vadim Ratner. Reduce discrepancy of human annotators in medical imaging by automatic visual comparison to similar cases, 2021. US Patent 10,916,343. 1
- [5] Christian F Baumgartner, Kerem C Tezcan, Krishna Chaitanya, Andreas M Hötter, Urs J Muehlematter, Khoschy Schawkat, Anton S Becker, Olivio Donati, and Ender Konukoglu. Phiseg: Capturing uncertainty in medical image segmentation. In *MICCAI 2019*, pages 119–127. Springer, 2019. 1
- [6] Alan Joseph Bekker and Jacob Goldberger. Training deep neural-networks based on unreliable labels. In *2016 IEEE International Conference on Acoustics, Speech and Signal Processing (ICASSP)*, pages 2682–2686, 2016. 2
- [7] J. C. Caicedo, A. Goodman, K. W. Karhohs, B. A. Cimini, J. Ackerman, M. Haghighi, C. Heng, T. Becker, M. Doan, C. McQuin, M. Rohban, S. Singh, and A. E. Carpenter. Nucleus segmentation across imaging experiments: The 2018 data science bowl. *Nature Methods*, vol. 16(no. 12):pp. 1247–1253, 2019. 1
- [8] Daniel C. Castro, Jeremy Tan, Bernhard Kainz, Ender Konukoglu, and Ben Glocker. Morpho-MNIST: Quantitative assessment and diagnostics for representation learning. *Journal of Machine Learning Research*, 20(178), 2019. 7, 8, 1
- [9] Geng Chen, Dehui Xiang, Bin Zhang, Haihong Tian, Xiaoling Yang, Fei Shi, Weifang Zhu, Bei Tian, and Xinjian Chen. Automatic pathological lung segmentation in low-dose ct image using eigenspace sparse shape composition. *IEEE Transactions on Medical Imaging*, 38(7):1736–1749, 2019. 2, 3
- [10] Xinlei Chen and Abhinav Gupta. Webly supervised learning of convolutional networks. In *Proceedings of the IEEE international conference on computer vision*, pages 1431–1439, 2015. 2
- [11] Li Deng. The mnist database of handwritten digit images for machine learning research. *IEEE Signal Processing Magazine*, 29(6):141–142, 2012. 6, 8
- [12] Jacob Goldberger and Ehud Ben-Reuven. Training deep neural-networks using a noise adaptation layer. In *ICLR*, 2017. 2
- [13] Melody Guan, Varun Gulshan, Andrew Dai, and Geoffrey Hinton. Who said what: Modeling individual labelers improves classification. In *AAAI*, 2018. 4
- [14] Bo Han, Quanming Yao, Xingrui Yu, Gang Niu, Miao Xu, Weihua Hu, Ivor Tsang, and Masashi Sugiyama. Co-teaching: Robust training of deep neural networks with extremely noisy labels. *Advances in neural information processing systems*, 31, 2018. 1, 3, 6
- [15] Dan Hendrycks, Mantas Mazeika, Duncan Wilson, and Kevin Gimpel. Using trusted data to train deep networks on labels corrupted by severe noise. In *NeurIPS*, pages 10456–10465, 2018. 2
- [16] Martin Holm Jensen, Dan Richter Jørgensen, Raluca Jalaboi, Mads Eiler Hansen, and Martin Aastrup Olsen. Improving uncertainty estimation in convolutional neural networks using inter-rater agreement. In *MICCAI 2019*, pages 540–548. Springer, 2019. 4
- [17] Songbai Ji, David W Roberts, Alex Hartov, and Keith D Paulsen. Combining multiple true 3d ultrasound image volumes through re-registration and rasterization. In *MICCAI 2009*, pages 795–802. Springer, 2009. 2, 3

- [18] Wei Ji, Shuang Yu, Junde Wu, Kai Ma, Cheng Bian, Qi Bi, Jingjing Li, Hanruo Liu, Li Cheng, and Yefeng Zheng. Learning calibrated medical image segmentation via multi-rater agreement modeling. In *CVPR*, pages 12341–12351, 2021. 7, 3, 8, 9
- [19] Lu Jiang, Zhengyuan Zhou, Thomas Leung, Li Jia Li, and Li Fei-Fei. In *ICML*, pages 3601–3620, 2018. 1, 2
- [20] Modat M Jorge Cardoso M, Leung K. Steps: Similarity and truth estimation for propagated segmentations and its application to hippocampal segmentation and brain parcellation. *Medical image analysis*, 17:671–84, 2013. 2, 3
- [21] Leo Joskowicz, D Cohen, N Caplan, and Jacob Sosna. Inter-observer variability of manual contour delineation of structures in ct. *European radiology*, 29:1391–1399, 2019. 1, 2
- [22] Alain Jungo, Raphael Meier, Ekin Ermis, Marcela Blatti-Moreno, Evelyn Herrmann, Roland Wiest, and Mauricio Reyes. On the effect of inter-observer variability for a reliable estimation of uncertainty of medical image segmentation. In *MICCAI 2018*, pages 682–690. Springer, 2018. 4
- [23] Eytan Kats, Jacob Goldberger, and Hayit Greenspan. A soft staple algorithm combined with anatomical knowledge. In *MICCAI 2019*, pages 510–517. Springer, 2019. 2, 3
- [24] Simon Kohl, Bernardino Romera-Paredes, Clemens Meyer, Jeffrey De Fauw, Joseph R Ledsam, Klaus Maier-Hein, SM Eslami, Danilo Jimenez Rezende, and Olaf Ronneberger. A probabilistic u-net for segmentation of ambiguous images. In *NeurIPS*, 2018. 4, 7, 8, 1, 9
- [25] Alex Krizhevsky, Geoffrey Hinton, et al. Learning multiple layers of features from tiny images. 2009. 6
- [26] Elizabeth Lazarus, Martha B Mainiero, Barbara Schepps, Susan L Koelliker, and Linda S Livingston. Bi-rads lexicon for us and mammography: interobserver variability and positive predictive value. *Radiology*, 239(2):385–391, 2006. 1
- [27] Ge Li, Changsheng Li, Chan Zeng, Peng Gao, and Guotong Xie. Region focus network for joint optic disc and cup segmentation. In *AAAI*, pages 751–758, 2020. 2, 3
- [28] Junnan Li, Richard Socher, and Steven CH Hoi. Dividemix: Learning with noisy labels as semi-supervised learning. In *International Conference on Learning Representations*, 2019. 3
- [29] Xuefeng Li, Tongliang Liu, Bo Han, Gang Niu, and Masashi Sugiyama. Provably end-to-end label-noise learning without anchor points. In *International Conference on Machine Learning*, pages 6403–6413. PMLR, 2021. 3, 7, 6
- [30] Xuefeng Liang, Xingyu Liu, and Longshan Yao. Review—A Survey of Learning from Noisy Labels. *ECS Sensors Plus*, 1(2):021401, 2022. 6
- [31] Geert Litjens, Thijs Kooi, Babak Ehteshami Bejnordi, Arnaud Arindra Adiyoso Setio, Francesco Ciompi, Mohsen Ghafoorian, Jeroen A.W.M. van der Laak, Bram van Ginneken, and Clara I. Sánchez. A survey on deep learning in medical image analysis. *Medical Image Analysis*, 42(1995): 60–88, 2017. 1
- [32] Quande Liu, Qi Dou, Lequan Yu, and Pheng Ann Heng. Msnet: Multi-site network for improving prostate segmentation with heterogeneous mri data. *IEEE Transactions on Medical Imaging*, 2020. 2, 3
- [33] Kede Ma, Xuelin Liu, Yuming Fang, and Eero P Simoncelli. Blind image quality assessment by learning from multiple annotators. In *2019 IEEE international conference on image processing (ICIP)*, pages 2344–2348. IEEE, 2019. 1, 6
- [34] Eran Malach and Shai Shalev-Shwartz. Decoupling “when to update” from “how to update”. *Advances in Neural Information Processing Systems*, 2017-Decem:961–971, 2017. 1, 2
- [35] Aditya Krishna Menon, Ankit Singh Rawat, Sashank J. Reddi, and Sanjiv Kumar. Can gradient clipping mitigate label noise? In *International Conference on Learning Representations*, 2020. 3
- [36] Zahra Mirikharaji, Yiqi Yan, and Ghassan Hamarneh. Learning to segment skin lesions from noisy annotations. In *First MICCAI Workshop, DART 2019, and First International Workshop, MIL3ID 2019*, pages 207–215. Springer, 2019. 3
- [37] Andriy Myronenko. 3d mri brain tumor segmentation using autoencoder regularization. In *4th International Workshop, BrainLes 2018, Held in Conjunction with MICCAI 2018*, pages 311–320. Springer, 2019. 2, 3
- [38] Giorgio Patrini, Alessandro Rozza, Aditya Krishna Menon, Richard Nock, and Lizhen Qu. Making deep neural networks robust to label noise: A loss correction approach. In *CVPR*, pages 2233–2241, 2017. 2
- [39] Scott E. Reed, Honglak Lee, Dragomir Anguelov, Christian Szegedy, Dumitru Erhan, and Andrew Rabinovich. Training deep neural networks on noisy labels with bootstrapping. In *ICLR 2015 - Workshop Track Proceedings*, pages 1–11, 2015. 2
- [40] Olaf Ronneberger, Philipp Fischer, and Thomas Brox. U-net: Convolutional networks for biomedical image segmentation. In *MICCAI 2015*, pages 234–241. Springer, 2015. 4
- [41] Mike Schaeckermann, Graeme Beaton, Minahz Habib, Andrew Lim, Kate Larson, and Edith Law. Understanding expert disagreement in medical data analysis through structured adjudication. In *Proceedings of the ACM Conference on Human-Computer Interaction*, pages 1–23, 2019. 2
- [42] Schilling, Marcel P.Scherr, Tim Munke, Friedrich R. Neumann, Oliver Schutera, Mark Mikut, Ralf Reischl, and Markus. A self-configuring method for deep learning-based biomedical image segmentation. *Radiology*, 18(2):203–211, 2021. 1
- [43] Amila Silva, Ling Luo, Shanika Karunasekera, and Christopher Leckie. Noise-robust learning from multiple unsupervised sources of inferred labels. In *AAAI*, pages 8315–8323, 2022. 3
- [44] Ryutaro Tanno, Ardavan Saeedi, Swami Sankaranarayanan, Daniel C Alexander, and Nathan Silberman. Learning from noisy labels by regularized estimation of annotator confusion. In *CVPR*, pages 11244–11253, 2019. 2, 3, 4, 5, 6, 1
- [45] Andreas Veit, Neil Alldrin, Gal Chechik, Ivan Krasin, Abhinav Gupta, and Serge Belongie. Learning from noisy large-scale datasets with minimal supervision. In *CVPR*, pages 839–847, 2017. 1

- [46] Simon Warfield, Kelly Zou, and William Wells. Simultaneous truth and performance level estimation (staple): An algorithm for the validation of image segmentation. *IEEE transactions on medical imaging*, 23:903–21, 2004. [2](#), [3](#)
- [47] Hongxin Wei, Lei Feng, Xiangyu Chen, and Bo An. Combating noisy labels by agreement: A joint training method with co-regularization. In *Proceedings of the IEEE/CVF conference on computer vision and pattern recognition*, pages 13726–13735, 2020. [1](#), [3](#), [6](#)
- [48] Jiaheng Wei, Zhaowei Zhu, Hao Cheng, Tongliang Liu, Gang Niu, and Yang Liu. Learning with noisy labels revisited: A study using real-world human annotations. In *International Conference on Learning Representations*, 2022. [6](#)
- [49] N. Wu, J. Phang, J. Park, Y. Shen, Z. Huang, M. Zorin, S. Jastrzebski, T. Févry, J. Katsnelson, E. Kim, and S. Wolfson. Deep neural networks improve radiologists’ performance in breast cancer screening. *IEEE Trans. Med. Imag.*, vol., vol. 39:pp. 1184–1194, 2020. [1](#)
- [50] Xiaobo Xia, Tongliang Liu, Nannan Wang, Bo Han, Chen Gong, Gang Niu, and Masashi Sugiyama. Are Anchor Points Really Indispensable in Label-Noise Learning? In *Advances in Neural Information Processing Systems*. Curran Associates, Inc., 2019. [2](#)
- [51] Xiaobo Xia, Tongliang Liu, Bo Han, Chen Gong, Nannan Wang, Zongyuan Ge, and Yi Chang. Robust early-learning: Hindering the memorization of noisy labels. In *International conference on learning representations*, 2020. [3](#), [6](#)
- [52] Han Xiao, Kashif Rasul, and Roland Vollgraf. Fashion-mnist: a novel image dataset for benchmarking machine learning algorithms. *arXiv preprint arXiv:1708.07747*, 2017. [6](#)
- [53] Yan Yan, Rómer Rosales, Glenn Fung, Ramanathan Subramanian, and Jennifer Dy. Learning from multiple annotators with varying expertise. *Machine Learning*, 95(3):291–327, 2014. [1](#)
- [54] Kun Yi and Jianxin Wu. Probabilistic end-to-end noise correction for learning with noisy labels. *Proceedings of the IEEE Computer Society Conference on Computer Vision and Pattern Recognition*, 2019-June:7010–7018, 2019. [3](#)
- [55] Xingrui Yu, Bo Han, Jiangchao Yao, Gang Niu, Ivor Tsang, and Masashi Sugiyama. How does disagreement help generalization against label corruption? In *International Conference on Machine Learning*, pages 7164–7173. PMLR, 2019. [1](#), [3](#), [6](#)
- [56] Le Zhang, Ryutaro Tanno, Mou Cheng Xu, Chen Jin, Joseph Jacob, Olga Ciccarelli, Frederik Barkhof, and Daniel C. Alexander. Disentangling human error from the ground truth in segmentation of medical images. In *NeurIPS*, pages 1–13, 2020. [2](#), [3](#), [4](#), [5](#), [7](#), [1](#), [6](#), [8](#), [9](#)
- [57] He Zhao, Huiqi Li, and Li Cheng. Improving retinal vessel segmentation with joint local loss by matting. *Pattern Recognition*, 98:107068, 2020. [2](#), [3](#)

## A. Proposed architecture for Segmentation

In this section, we introduce the problem of training a segmentation model in the presence of multiple annotations. Since each of the annotations is received from some expert with his expertise and biases, we consider these annotations as “noisy”.

We assume our training dataset  $\mathcal{D}$  is a collection of  $N$  input images and their corresponding noisy annotations received from a subset of fixed annotators. By  $S(x_i)$ , we denote the set of indices of those annotators who provided their annotations for an input image  $x_i$ . We assume that overall we have  $R$  annotators, and their identities are preserved for all the images.

The dataset therefore has the following structure:  $\mathcal{D} = \{x_i, \{\tilde{y}_i^r\}_{r \in S(x_i)}\}_{i=1}^N$ , where  $\tilde{y}_i^r$  corresponds to an annotation of  $r$ -th expert for the input image  $x_i$ . The tilde sign reminds us that the annotation is noisy. Each image and corresponding annotations have the following shapes:  $x_i \in \mathbb{R}^{W \times H \times C}$  and  $\tilde{y}_i^r \in \mathcal{Y}^{W \times H}$ , where  $W, H, C$  are width, height and a number of channels correspondingly, and  $\mathcal{Y} = [1, 2, \dots, L]$  is a set of possible class labels.

It is worth noting that the ground truth segmentation annotations  $y_i$  are not available to us but assumed to exist. Thus, our goal is to build a model which will approximate the true distribution of class labels  $p(y_i | x_i)$  for a given input solely from the dataset of noisy annotations.

### A.1. Probabilistic Model for Noisy Observations and Architecture

In this section, we build a probabilistic noise model for observed noisy annotations. Following [44, 56], we assume statistical independence of annotators and independence of annotations of different pixels for a given input image  $x_i$ .

For the following derivations, we will omit the object index  $i$  to simplify the notation. Taking these assumptions into account, we can write the joint likelihood for all annotations  $\{\tilde{y}^r\}_{r \in S(x)}$  of a given input image  $x$ :

$$p(\{\tilde{y}^r\}_{r \in S(x)} | x) = \prod_{r \in S(x)} p(\tilde{y}^r | x) \quad (6)$$

$$= \prod_{r \in S(x)} \prod_{w=1}^W \prod_{h=1}^H p(\tilde{y}_{wh}^r | x),$$

where  $\tilde{y}_{wh}^r$  is a class label of a pixel in a specific location.

Each of the probabilities  $p(\tilde{y}_{wh}^r | x)$  inside the product is an implicit marginalization of the latent ground truth class label  $y_{wh}$ :

$$p(\tilde{y}_{wh}^r | x) = \sum_{l=1}^L p(y_{wh} = l | x) p(\tilde{y}_{wh}^r | y_{wh} = l, x). \quad (7)$$

In this equation, we see that the predictive distribution for a noisy annotation is a mixture of class-conditional distributions of noisy annotations weighed by the ground truth label distributions. These noisy class conditional distributions can be considered as elements of a confusion matrix (CM), effectively modeling the noise introduced by the an-

notator.

Inspired by [44, 56], we use a two-component model to approximate the densities in equation (2). The first component is the segmentation network, and the other is an annotation network. The segmentation network is a convolutional neural network parameterized by  $\theta$  that aims to approximate the ground truth probability distribution  $p(y_{wh} | x)$ . Hence, it transforms an input image  $x$  to a probability map  $\hat{p}_\theta(x) \in \mathbb{R}^{W \times H \times L}$ , where each  $(wh)$ -th element approximates  $p(y_{wh} | x)$ .

The annotation network, parameterized by  $\psi$ , provides pixel-wise estimates of the CMs of the corresponding annotators as a function of the input image. Hence, this model, trained separately for each of the annotators, produces the tensor  $\hat{T}_\psi^r(x) \in [0, 1]^{W \times H \times L \times L}$ ,  $r \in S(x)$ . The element of this tensor, indexed by  $whkl$ , equals to  $p(\tilde{y}_{wh}^r = k | y_{wh} = l, x)$ .

The multiplication of these two terms  $\hat{p}_{\theta, \psi}^r(x) = \hat{T}_\psi^r(x) \times \hat{p}_\theta(x)$  resulting in the tensor of shape  $W \times H \times L$ , is the  $r$ -th annotator’s probability segmentation map which is optimized in the loss function (the details are covered in Section 4.1). The architecture of the resulting model is depicted in Figure 5.

## B. Datasets

### B.1. Segmentation Datasets

In this section, we describe and illustrate the data we use to train our model for the segmentation task.

**MNIST.** It is the database of handwritten digits that is used as an example of a dataset with artificial noises. This dataset is used to show the performance of the model in cases where ground truth is known. Synthetic annotations are created by applying morphological transformations simulations on assumed ground truth [8]. The types of annotators from the simulation are thin (under-segmentation), thick (over-segmentation), fracture (fracture-segmentation), and good (ground truth). For our purpose, we only use the first three annotations. In addition, Gaussian noise was added to the original images to use them as inputs for the model. There are 60,000 samples for training and 10,000 data samples reserved for testing. In Figure 6, we show different augmentations for the MNIST dataset, artificially creating several annotators.

**LIDC-IDRI.** The lung image database consortium (LIDC) and image database resource initiative (IDRI) is a completed reference database of lung nodules on CT scans [2]. It consists of 1,018 3D thorax CT scans with 4 annotations from four radiologists. For pre-processing, we used the same method in [24], which provides 15,096 2D slices, and used the 60-20-20 dataset split as done in [5]. In

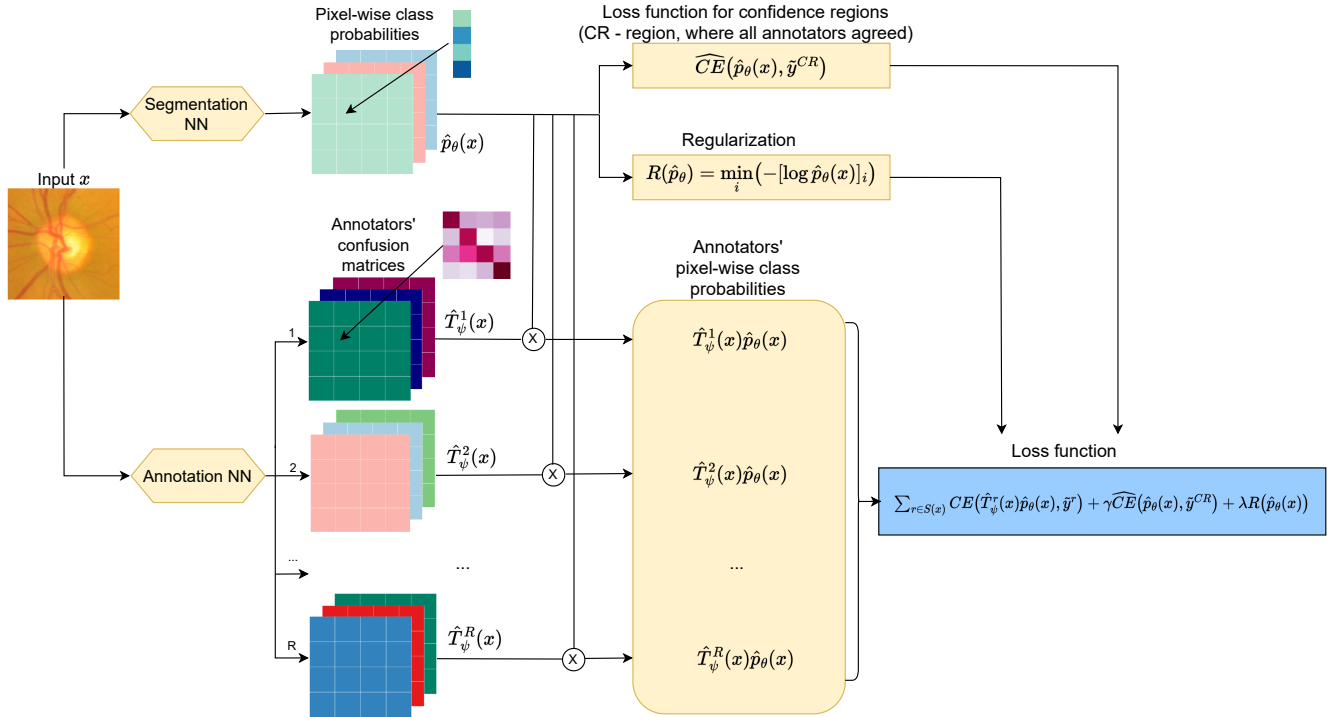


Figure 5. Illustration of the proposed architecture. The input image is fed into two separate networks – Segmentation and Annotation. Then, their predictions are multiplied to produce the prediction of the noisy (annotators) segmentation masks. Finally, the loss function is computed, summing up all the components.

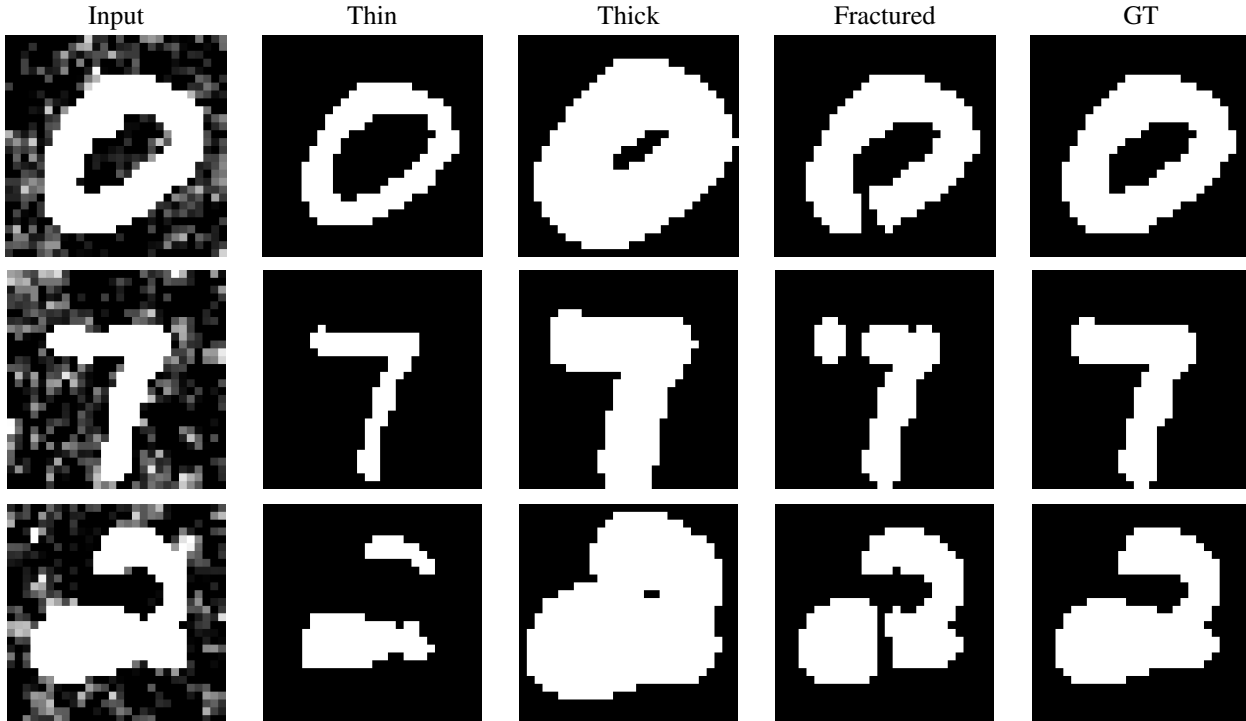


Figure 6. Visualization of the MNIST dataset input image with Gaussian noise, three annotations (thin, thick, fracture), and ground truth.

Figure 7, we illustrate the input image with annotations, as well as our predicted results for the LIDC dataset.

**RIGA.** Retinal fundus images for glaucoma analysis (RIGA) dataset contains 750 original images and 4,500 annotations and was collected from three sources: BinRushed (195 images), MESSIDOR (460 images), and Magrabia (95 images) [1]. 4,500 annotations came from six experienced ophthalmologists, who manually labeled the optic cup/disc boundaries for each image. For model training, we used samples from BinRushed and MESSIDOR and used samples from Magrabia as a test set. For the image preprocessing, we followed the settings in [18] by resizing to  $256 \times 256$ , and then we normalized each pixel by subtracting the mean and dividing by the standard deviation, which is calculated on training data. In Figure 8, we illustrate the input image, annotator masks, and boundaries of different annotators for the RIGA dataset.

## B.2. Classification Datasets

In this section, we describe the data and types of noises we use to train our model for the classification task.

**MNIST.** As described in Appendix B.1, dataset comprise of 60,000 samples for training, and 10,000 data samples reserved for testing. The number of classes in the dataset is 10.

**CIFAR-10.** The CIFAR-10 dataset contains 60,000 color images in 10 classifications, with 6000 images in each class. There are 50,000 training and 10,000 test images. The dataset is divided into five training batches and one test batch, each contains 10,000 images. The test batch is a collection of exactly 1,000 data samples randomly selected from each class. The training batches comprise of the remaining images in a random order, however it’s likely that certain training batches may have more images from one class than another.

**CIFAR-10N.** CIFAR-10N is prepared by augmenting the training datasets of CIFAR-10 using Amazon Mechanical Turk-collected human-annotated real-world noisy labels. It has the same number of classes and training and test data points as CIFAR-10 dataset.

**FMNIST.** Fashion-MNIST is a dataset of article images from Zalando. It consists of a training set of 60,000 instances and a test set of 10,000 instances. Each instance is a  $28 \times 28$  grayscale image with a label from one of ten classes.

## B.2.1 Types of Noise

We simulated the noise in our datasets by confusing each class with another class and assigning the probability proportion for corrupting the labels. Figure 9 shows the examples of noise transition matrices for pairflip 20% and symmetric 50% noise types. In addition, Figure 10 signifies the noise labels distributions for CIFAR-10 dataset for pairflip 45% and symmetric 50% noise types; this distribution of the label noise is used in the training process.

## C. Supplementary Results

In this section, we provide supplementary visualizations for trained segmentation models. In the following subsections, we discuss the results for each dataset in more detail, computing the Dice coefficients separately for each of the classes.

### C.1. Segmentation

Along the Dice coefficient between the prediction  $\hat{p}_\theta(x)$  and true label  $y$ , we also consider following Dice coefficients:

- $D(y_a, y_a)$  is the average Dice coefficient among the noisy annotations  $y_a$ . This shows how raters are in agreement among themselves. First, the Dice coefficient between  $i^{th}$  and  $j^{th}$  ( $i \neq j$ ) annotations are calculated, and the average value is taken from all possible combinations. Similarly, the Dice coefficient among predictions of annotations  $D(\tilde{y}_a, \tilde{y}_a)$  calculated to show the agreement/disagreement level among the predictions. If these two measures are close, we did a good job of predicting annotations.
- $D(\tilde{y}_a, y_a)$  is a Dice coefficient between the annotations’ predictions and noisy labels. The Dice coefficient between the annotations  $y_a^i$  and its corresponding prediction  $\tilde{y}_a^i$  ( $i = 1, \dots, R$ ) is calculated first and then averaged. This measures how correctly the annotations were modeled.
- $D(y_a, y_{gt})$  is a Dice coefficient between noisy labels and true labels. First, it was calculated for the rater and averaged over all raters. This shows each rater’s agreement/disagreement with the true label. Similarly, the Dice coefficient between the annotations’ predictions and true label  $D(\tilde{y}_a, y_{gt})$  is calculated. The expectation is that these values will be close.
- $D(\tilde{y}, y_{gt})$  if the Dice coefficient between the main output (prediction of the true label) and true label.

We tuned relative weight hyperparameters such as learning rate,  $\lambda, \gamma$  for segmentation model using automatic tool (wandb.ai) for the results in the main text and ablation study in Section C.2. Then, we picked the best values in terms of the Dice score between predicted and true labels.

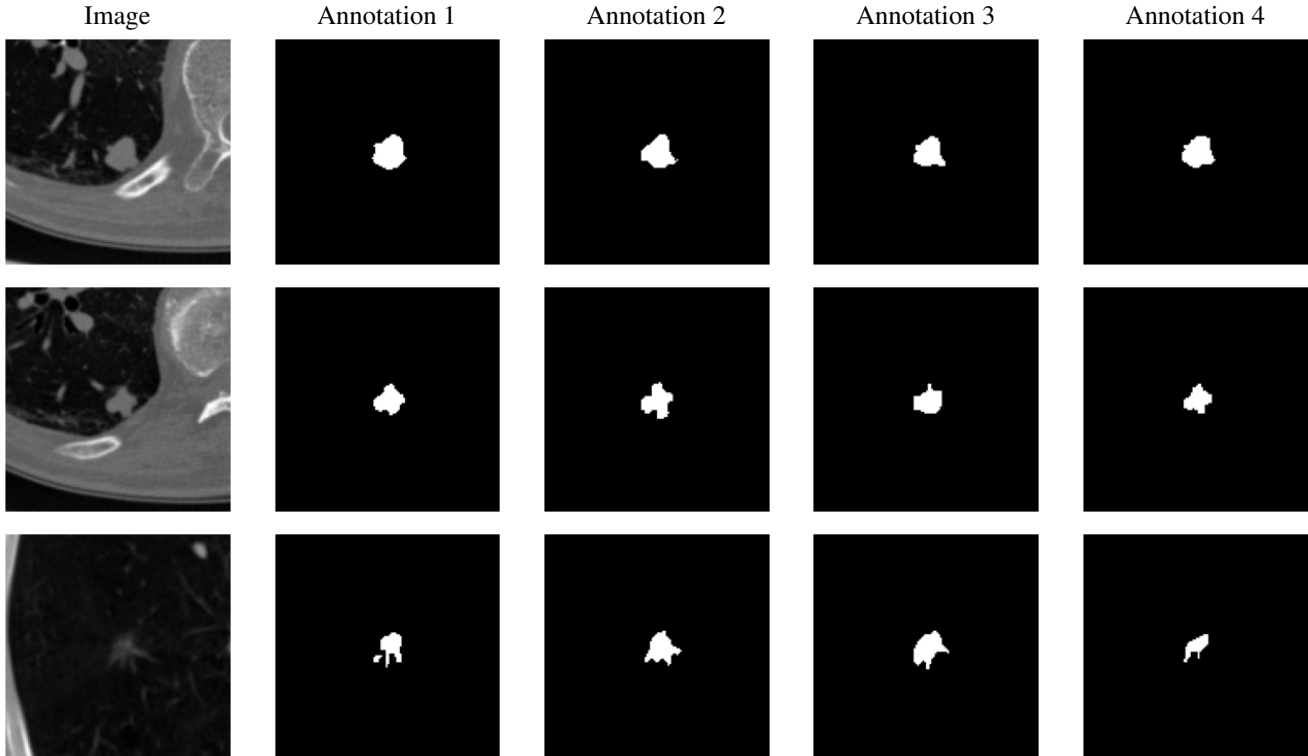


Figure 7. Visualization of LIDC dataset input image and its all annotations.

**MNIST.** The Dice coefficients for all six classes of the MNIST dataset are depicted in Table 6. In this context, class 0 denotes the background, while class 1 signifies the numbers. We observe that our approach, augmented with a confidence regularizer, consistently yields the highest or second-best performance in terms of class-wise Dice coefficients when applied to the MNIST dataset. To further illustrate these results, we have included additional visualizations of the final segmentations achieved on the MNIST dataset as depicted in Figure 11.

**LIDC.** The Dice coefficients for all six classes within the LIDC dataset are presented in Table 7. Within this dataset, class 0 corresponds to the background, while class 1 denotes the lung. As demonstrated by the results, our model with the confidence regularizer typically outperforms the competitors. Interestingly, even in the absence of the confidence regularizer, our method outperforms other models by a substantial margin for class 1. To provide a more detailed comparison, we have included examples of predictions made by our model and true label (taken as majority vote) in Figure 12.

**RIGA.** The performance metrics for the RIGA dataset are presented in Table 8. In this context, class 0 corresponds to

the background, class 1 is the optical disc, and class 2 is the optical cup. Our models show robust performance for classes 0 and 1 on this dataset and achieve the highest score for class 2. Interestingly, the application of confidence regularization consistently yields superior results. Intriguingly, in this particular instance, the variance of the Dice coefficient for our model is notably smaller in comparison to other methods, underscoring the stability of our approach. For a more detailed visual insight, please refer to Figure 13 and Figure 14.

## C.2. Comparative Analysis of Various Regularizers for Segmentation.

This section is dedicated to a comparative analysis of various regularizers applied to the same architecture type, namely segmentation and annotation networks; and the dilation procedure (see Table 9 below). The goal of this ablation study is to assess the individual and collective impact of these regularizers on real-world image segmentation datasets, thereby emphasizing the importance of the regularizer choice in such models. We observe that having both loss terms we proposed is critical to achieving high-quality results. Interestingly, we see that for the LIDC dataset, one can slightly improve the results further by tuning the dilation procedure.

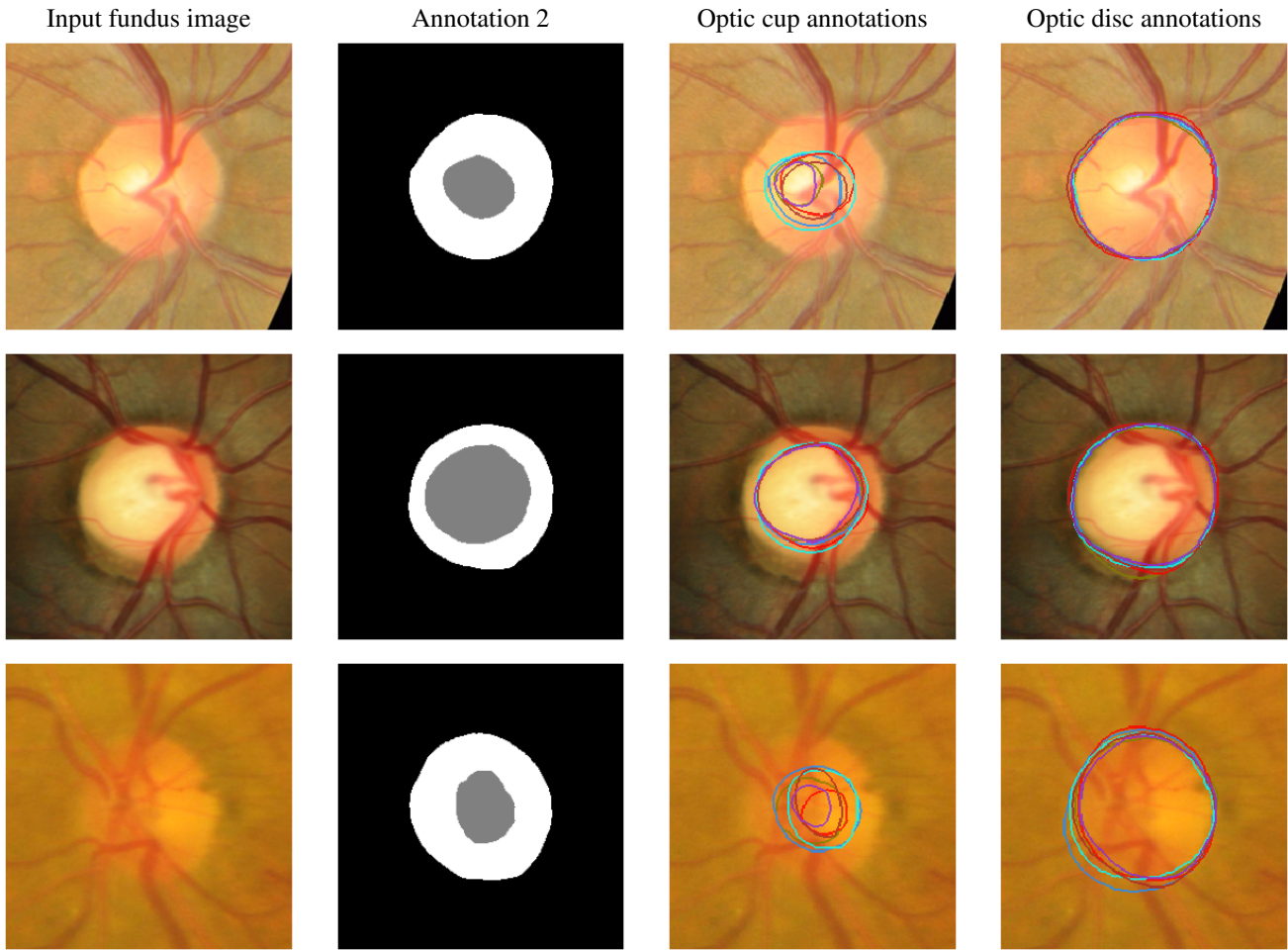


Figure 8. Visualization of the RIGA dataset from left to right: input image, one of the annotations, boundaries of all six annotations for cup, and boundaries of all six annotations for the disc.

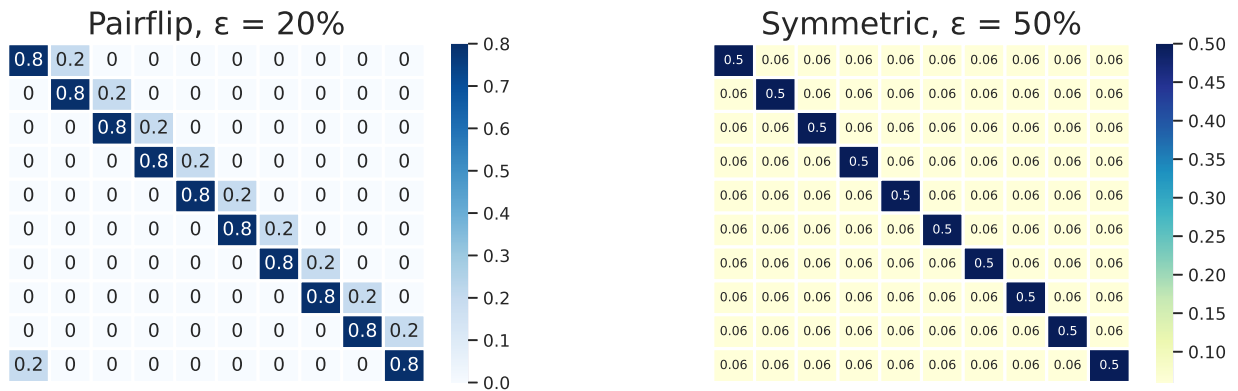


Figure 9. Noise Transition matrices for Pairflip and Symmetric noise.



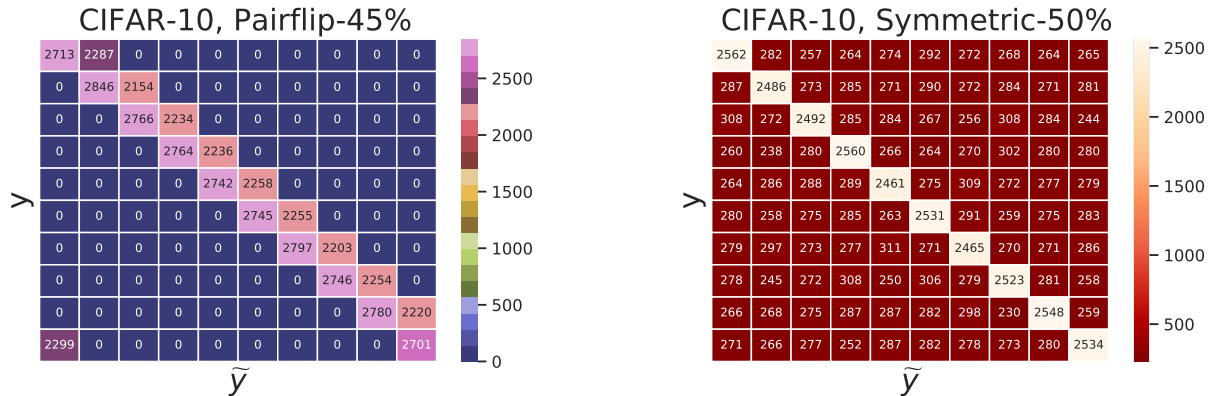


Figure 10. Confusion matrix between clean ( $y$ ) and noisy labels ( $\tilde{y}$ ) of CIFAR-10 dataset for (a) Pairflip-45% and (b) Symmetric-50% noise.

The results of our analysis, which are summarized in Table 9, consider several regularizers. Among these are the CM-Net [56] and the Logdet [29], in addition to other combinations. Our intention was to compare these well-established regularizers against the one we propose in this study.

Notably, the table reveals that our proposed regularizer, which includes an additional term for confident regions, exceeds the performance of the other options by a considerable margin. This superior performance may be attributed to the fact that our proposed regularizer does not impose any additional constraints on the parameters. For instance, it does not enforce diagonal dominance as in the Logdet [29], a requirement that is explicitly stated. Neither does it employ the same constraints as those theoretically proven in CM-Net [56], whose practical implementation in the algorithm and code remains somewhat ambiguous.

In conclusion, these results highlight the potential benefits of our proposed regularizer within the context of medical image segmentation.

### C.3. Classification

**MNIST.** We used a LeNet model as a classifier for our backbone network. For the annotator network, we have a linear layer of size  $C \times C$ ,  $C$  denotes the number of classes. This linear layer represents our annotator confusion matrices, and we apply a softmax layer to it to make it a stochastic matrix along a certain dimension. We fine-tuned our model for a combination of learning rates,  $\alpha = [0.01, 0.001, 0.0001, 0.000001, 0.0016, 0.008, 0.0064, 0.005]$ , and about 50 different lambda values,  $\lambda$ , for our regularizer hyper-parameter. We started with a very small value of  $\lambda = 0.001506746$ , and slowly increased it exponentially (geometric progression) per epoch with a rate,  $r = 1.18$ ; we trained the model for 70 epochs and used Adam as an opti-

mizer. In addition, the experiments were regulated to assess the performance of the model when the confusion matrix is initialized as an identity. These fine-tunings are done across all 2 different types of noise described in Section 5.2.3 with the respective noise rate that is associated with each of the noise types.

Table 10 shows the performance comparison of our algorithm with the other methods. The results of the our methodology with entropy and information-based regularizers are superior compared to other method, specially for more challenging cases of higher noise rates.

In Figure 15, we highlight the test accuracy vs. number of epochs. We can see clearly that for symmetric noise types, all algorithms gave comparable performance. It can be clearly seen that for symmetric noise, our test accuracy starts to decline a bit. This could be alleviated with an early stopping criteria which was not incorporated in these experiments. For pairflip 45%, the test accuracy starts to increase and stabilize in the later epochs of the experiment and transcends all the baselines.

**CIFAR-10.** For CIFAR-10, we used ResNet-18 as our backbone network for the classifier. The annotator network remains unchanged (still has one linear layer that represents the confusion matrices of class  $C \times C$  that are stochastic). For this dataset, we fine-tuned the model for an assortment of learning rates, such as  $\alpha = [0.001, 0.00064, 0.0016, 0.000001, 0.005, 0.008, 0.0016, 0.00064]$ . We ran the model for 150 epochs; the hyperparameter  $\lambda$  for our regularizer was slowly increased exponentially again with a rate,  $r = 1.11$ . However, the starting value this time is  $\lambda = 3.0517578125e-05$ . We used a standard batch-size,  $BS=128$ . We used the standard augmentations of random crop of size  $32 \times 32$  and horizontal random flipping. These are the standard augmentations that have been used across

		$D(\tilde{y}_a, \tilde{y}_a)$	$D(y_a, y_a)$	$D(\tilde{y}_a, y_a)$	$D(\tilde{y}_a, y_{gt})$	$D(y_a, y_{gt})$	$D(\tilde{y}, y_{gt})$
<b>MR-Net</b> [18]	class 0	91.08	90.90	98.34	95.03	95.34	<u>98.20</u>
		$\pm 0.49$	$\pm 0.00$	$\pm 0.04$	$\pm 0.23$	$\pm 0.00$	$\pm 0.19$
	class 1	72.48	71.80	94.15	84.16	85.25	<u>93.43</u>
		$\pm 0.89$	$\pm 0.00$	$\pm 0.11$	$\pm 0.60$	$\pm 0.00$	$\pm 0.72$
<b>PU-Net</b> [24]	class 0	93.78	90.90	95.22	95.02	95.34	94.92
		$\pm 0.43$	$\pm 0.00$	$\pm 0.26$	$\pm 0.43$	$\pm 0.00$	$\pm 0.88$
	class 1	78.68	71.80	94.35	82.99	82.25	82.31
		$\pm 1.14$	$\pm 0.00$	$\pm 0.19$	$\pm 0.71$	$\pm 0.00$	$\pm 0.85$
<b>CM-Net</b> [56]	class 0	91.10	90.90	98.54	95.11	95.34	97.17
		$\pm 0.12$	$\pm 0.00$	$\pm 0.00$	$\pm 0.06$	$\pm 0.00$	$\pm 0.01$
	class 1	72.45	71.80	94.88	84.44	85.25	90.52
		$\pm 0.04$	$\pm 0.00$	$\pm 0.01$	$\pm 0.09$	$\pm 0.00$	$\pm 0.03$
<b>Ours</b>	class 0	91.00	90.90	98.47	95.05	95.34	<b>98.49</b>
		$\pm 0.10$	$\pm 0.00$	$\pm 0.01$	$\pm 0.05$	$\pm 0.00$	$\pm 0.02$
	class 1	72.30	71.80	94.69	84.32	85.25	<b>94.72</b>
		$\pm 0.31$	$\pm 0.00$	$\pm 0.02$	$\pm 0.16$	$\pm 0.00$	$\pm 0.06$
<b>Ours (No Confidence)</b>	class 0	91.01	90.90	98.47	95.05	95.34	97.39
		$\pm 0.08$	$\pm 0.00$	$\pm 0.01$	$\pm 0.04$	$\pm 0.00$	$\pm 0.01$
	class 1	72.29	71.80	94.69	84.31	85.25	91.56
		$\pm 0.13$	$\pm 0.00$	$\pm 0.02$	$\pm 0.16$	$\pm 0.00$	$\pm 0.03$

Table 6. Comparison of segmentation Dice coefficient (%) (mean  $\pm$  standard deviation) for MNIST, computed separately for each class. **Best** results are in bold, second-best underlined. The red column is the most interesting – the Dice coefficient between approximated and “real” ground-truth masks.

all the baselines that we have evaluated. The remaining settings remain the same as described in MNIST above.

Figure 16 shows the illustrative results of test accuracy vs. number of epochs. In all the three plots, it can be clearly seen that our algorithm performs at par with the other algo-

rithms, but the performance gets robustly superior in the extreme noise type of pairflip 45%. This shows that our method is particularly robust against harder noise as it is able to make confident predictions.

		$D(\tilde{y}_a, \tilde{y}_a)$	$D(y_a, y_a)$	$D(\tilde{y}_a, y_a)$	$D(\tilde{y}_a, y_{gt})$	$D(y_a, y_{gt})$	$D(\tilde{y}, y_{gt})$
<b>MR-Net</b> [18]	class 0	99.99	99.83	99.84	99.59	99.86	<b>99.85</b>
		$\pm 0.002$	$\pm 0.00$	$\pm 0.01$	$\pm 0.01$	$\pm 0.00$	$\pm 0.02$
	class 1	92.08	53.02	46.16	23.18	53.39	45.62
		$\pm 1.45$	$\pm 0.00$	$\pm 1.48$	$\pm .43$	$\pm 0.00$	$\pm 9.75$
<b>PU-Net</b> [24]	class 0	99.96	99.83	99.53	99.79	99.86	99.73
		$\pm 0.007$	$\pm 0.00$	$\pm 0.04$	$\pm 0.06$	$\pm 0.00$	$\pm 0.09$
	class 1	91.48	53.02	28.89	43.39	53.39	43.92
		$\pm 1.65$	$\pm 0.00$	$\pm 1.53$	$\pm 1.54$	$\pm 0.00$	$\pm 1.25$
<b>CM-Net</b> [56]	class 0	99.96	99.83	99.42	99.50	99.86	99.38
		$\pm 0.01$	$\pm 0.00$	$\pm 0.03$	$\pm 0.03$	$\pm 0.00$	$\pm 0.04$
	class 1	99.07	53.02	32.09	47.17	53.39	46.12
		$\pm 0.20$	$\pm 0.00$	$\pm 0.75$	$\pm 1.24$	$\pm 0.00$	$\pm 1.30$
<b>Ours</b>	class 0	99.89	99.83	99.44	99.52	99.86	<u>99.82</u>
		$\pm 0.05$	$\pm 0.00$	$\pm 0.09$	$\pm 0.09$	$\pm 0.00$	$\pm 0.02$
	class 1	99.18	53.02	31.43	46.21	53.39	<b>64.33</b>
		$\pm 2.28$	$\pm 0.00$	$\pm 1.78$	$\pm 3.05$	$\pm 0.00$	$\pm 1.82$
<b>Ours (No Confidence)</b>	class 0	100.00	99.83	99.57	99.65	99.86	99.65
		$\pm 0.00$	$\pm 0.00$	$\pm 0.02$	$\pm 0.02$	$\pm 0.00$	$\pm 0.02$
	class 1	100.00	53.02	35.09	52.20	53.39	<u>52.20</u>
		$\pm 0.00$	$\pm 0.00$	$\pm 0.70$	$\pm 1.05$	$\pm 0.00$	$\pm 1.05$

Table 7. Comparison of segmentation Dice coefficient (%) (mean  $\pm$  standard deviation) for LIDC, computed separately for each class. **Best** results are in bold, second-best underlined. The red column is the most interesting – the Dice coefficient between approximated and “real” ground-truth masks.

**Fashion-MNIST.** We kept the same settings of CIFAR-10, such as ResNet-18 model and batch-size of 128 for Fashion-MNIST dataset. The model was again fine-tuned for the same set of hyperparameters. However, the starting value of  $\lambda = 6.103515625e-05$ , and it was increased expo-

nentially with a rate of  $r=1.12$ . We also retained the same set of augmentations that we used in CIFAR-10 dataset.

Figure 17 gives an illustrative result of test accuracy vs. number of epochs on Fashion-MNIST dataset. It showcases the test performance of our algorithm in comparison with

		$D(\tilde{y}_a, \tilde{y}_a)$	$D(y_a, y_a)$	$D(\tilde{y}_a, y_a)$	$D(\tilde{y}_a, y_{gt})$	$D(y_a, y_{gt})$	$D(\tilde{y}, y_{gt})$
<b>MR-Net</b> [18]	class 0	99.70	98.96	99.19	99.47	99.35	99.50
		$\pm 0.01$	$\pm 0.00$	$\pm 0.04$	$\pm 0.40$	$\pm 0.00$	$\pm 0.02$
	class 1	95.75	89.04	91.54	93.26	93.22	<b>93.97</b>
		$\pm 0.76$	$\pm 0.00$	$\pm 0.26$	$\pm 0.25$	$\pm 0.00$	$\pm 0.50$
	class 2	85.16	78.03	81.06	81.82	86.22	<u>86.16</u>
		$\pm 2.01$	$\pm 0.00$	$\pm 2.54$	$\pm 2.62$	$\pm 0.00$	$\pm 2.92$
<b>PU-Net</b> [24]	class 0	99.88	98.96	99.19	99.52	99.35	<b>99.60</b>
		$\pm 0.05$	$\pm 0.00$	$\pm 0.18$	$\pm 0.89$	$\pm 0.00$	$\pm 0.23$
	class 1	91.73	89.04	90.59	90.96	93.22	90.90
		$\pm 0.89$	$\pm 0.00$	$\pm 0.45$	$\pm 0.35$	$\pm 0.00$	$\pm 0.83$
	class 2	78.67	78.03	80.68	83.36	86.22	80.55
		$\pm 1.09$	$\pm 0.00$	$\pm 1.48$	$\pm 1.59$	$\pm 0.00$	$\pm 0.87$
<b>CM-Net</b> [56]	class 0	99.58	98.96	98.93	99.10	99.35	99.07
		$\pm 0.07$	$\pm 0.00$	$\pm 0.06$	$\pm 0.06$	$\pm 0.00$	$\pm 0.10$
	class 1	93.78	89.04	89.29	90.34	93.22	90.21
		$\pm 0.51$	$\pm 0.00$	$\pm 0.47$	$\pm 0.47$	$\pm 0.00$	$\pm 0.78$
	class 2	84.47	78.03	78.87	79.84	86.22	80.80
		$\pm 2.42$	$\pm 0.00$	$\pm 0.97$	$\pm 1.23$	$\pm 0.00$	$\pm 1.36$
<b>Ours</b>	class 0	99.54	98.96	99.07	99.24	99.35	<u>99.33</u>
		$\pm 0.05$	$\pm 0.00$	$\pm 0.02$	$\pm 0.30$	$\pm 0.00$	$\pm 0.01$
	class 1	94.04	89.04	90.76	91.80	93.22	<u>93.63</u>
		$\pm 0.40$	$\pm 0.00$	$\pm 0.19$	$\pm 0.25$	$\pm 0.00$	$\pm 0.07$
	class 2	84.05	78.03	81.52	82.21	86.22	<b>88.58</b>
		$\pm 1.63$	$\pm 0.00$	$\pm 0.61$	$\pm 0.96$	$\pm 0.00$	$\pm 0.25$
<b>Ours (No Confidence)</b>	class 0	99.62	98.96	99.05	99.24	99.35	99.26
		$\pm 0.05$	$\pm 0.00$	$\pm 0.01$	$\pm 0.02$	$\pm 0.00$	$\pm 0.03$
	class 1	94.02	89.04	90.56	91.62	93.22	92.18
		$\pm 0.42$	$\pm 0.00$	$\pm 0.15$	$\pm 0.27$	$\pm 0.00$	$\pm 0.49$
	class 2	83.78	78.03	82.09	82.56	86.22	84.75
		$\pm 2.15$	$\pm 0.00$	$\pm 0.66$	$\pm 1.23$	$\pm 0.00$	$\pm 1.29$

Table 8. Comparison of segmentation Dice coefficient (%) (mean  $\pm$  standard deviation) for RIGA, computed separately for each class. **Best** results are in bold, second-best underlined. The red column is the most interesting – the Dice coefficient between approximated and “real” ground-truth masks.

		Ours (R=4), Reg-Y, CR-Y	Ours (R=4), Reg-Y, CR-N	Ours (R=4), Reg-N, CR-Y	Ours (R=4), Reg-N, CR-N	CM-Net	LogDet	LogDet + Ours	Ours: R=3	Ours: R=5
RIGA	mean	<b>93.85</b>	92.06	91.43	75.8	90.03	<u>93.31</u>	92.99	92.14	91.17
	std	$\pm 0.09$	$\pm 0.58$	$\pm 0.25$	$\pm 0.47$	$\pm 0.91$	$\pm 0.11$	$\pm 0.26$	$\pm 0.12$	$\pm 0.58$

		Ours (R=2), Reg-Y, CR-Y	Ours (R=2), Reg-Y, CR-N	Ours (R=2), Reg-N, CR-Y	Ours (R=2), Reg-N, CR-N	CM-Net	LogDet	LogDet + Ours	Ours: R=1	Ours: R=3
LIDC	mean	<u>82.07</u>	75.93	79.48	75.31	72.75	77.38	77.58	<b>82.82</b>	80.92
	std	$\pm 0.92$	$\pm 0.53$	$\pm 0.38$	$\pm 1.14$	$\pm 0.66$	$\pm 0.69$	$\pm 0.69$	$\pm 0.21$	$\pm 0.41$

Table 9. In this table we present additional ablation results. Average Dice score with standard deviation over 10 last epochs, computed for different combinations of regularizers. Reg-(Y/N) means whether we apply (Y) our new regularizer or not (N). CR-(Y/N) means the same for the confidence region term on the loss function. The symbol “R” represents the count of dilation iterations. In the last two columns, we keep Reg-Y and CR-Y, while varying the number of dilation iterations. The **bold** results highlight the top performances, while the underlined ones signify the next best outcomes.

Noise rate	Ours-Inf	Ours-Ent	Co-tea.	Co-tea.+	JoCoR	Trace	CDR
symmetric 20%	<u>99.20</u>	<b>99.48</b>	99.01	98.88	98.82	99.16	98.97
	$\pm 0.20$	$\pm 0.23$	$\pm 0.02$	$\pm 0.02$	$\pm 0.03$	$\pm 0.21$	$\pm 0.02$
symmetric 30%	<b>99.11</b>	<u>99.09</u>	98.78	98.38	98.40	99.01	98.75
	$\pm 0.34$	$\pm 0.38$	$\pm 0.03$	$\pm 0.02$	$\pm 0.02$	$\pm 0.43$	$\pm 0.02$
symmetric 50%	<b>98.94</b>	<u>98.93</u>	92.24	95.26	96.83	98.87	97.72
	$\pm 0.77$	$\pm 0.81$	$\pm 0.02$	$\pm 0.03$	$\pm 0.04$	$\pm 0.80$	$\pm 0.02$
pairflip 20%	99.08	<b>99.55</b>	98.84	98.59	98.89	<u>99.13</u>	98.88
	$\pm 0.10$	$\pm 0.15$	$\pm 0.02$	$\pm 0.01$	$\pm 0.04$	$\pm 0.19$	$\pm 0.01$
pairflip 30%	98.94	<b>99.54</b>	98.57	97.95	98.56	<u>99.08</u>	98.50
	$\pm 0.17$	$\pm 0.20$	$\pm 0.02$	$\pm 0.01$	$\pm 0.04$	$\pm 0.13$	$\pm 0.01$
pairflip 45%	<u>98.77</u>	<b>99.10</b>	87.63	71.36	85.86	97.95	87.04
	$\pm 0.39$	$\pm 0.35$	$\pm 0.04$	$\pm 0.06$	$\pm 0.05$	$\pm 1.09$	$\pm 0.63$

Table 10. Comparison of test accuracy (%) (mean  $\pm$  st. dev.) for MNIST. **Best** results are in bold, second-best underlined.

other baselines. We can see that for all noise instances, our algorithm performs at par with the high achieving method like JoCoR. We perform considerably better against sample selection methods like Co-teaching and Co-teaching+, as well as against other method like CDR in the instance of pairflip 45%.

In addition, Figure 18 highlights the confusion matrices of the true class and the predicted class by the classifier network of our algorithm. We show the confusion matrices plots for two extreme noise types pairflip 45% and symmetric 50% for all the datasets used. It is clearly seen that the confusion matrices are diagonally dominant thus highlighting the robust performance of our method.

**CIFAR-10N.** We kept the same backbone architecture and fine-tune settings as CIFAR-10 in Section C.3.

### C.3.1 Additional experimental results

In our earlier experiments, we kept the same type of noise and noise levels across all the number of annotators in the

annotator network. This is usually not representative of the noise in the real world data, as it is possible that each annotator would be independent in the way it is confused about labelling and annotating the data (subject to their own biases). Therefore, we confuse each annotator with different types and levels of noise. Table 11 shows the test accuracy of the classifier network on CIFAR-10, Fashion-MNIST and MNIST datasets for different types of noise for each annotators. We achieved comparable results with an accuracy of 84.12%, 91.12% and 98.97% for CIFAR-10, Fashion-MNIST and MNIST respectively. It’s particularly notable that the accuracy of the classifier network remains at par even with using high level noise, such as pairflip 45% and symmetric 50% for two of the three annotators.

### C.3.2 MNIST Curated Dataset

In addition to symmetric and pairflip noises described in Section 5.2.3, we also consider asymmetric and pairflip with permutation noises. In the latter, the ordered label categories were first permuted randomly and labels of two ad-

CIFAR-10	Fashion-MNIST	MNIST
84.12	91.62	98.97
$\pm 0.34$	$\pm 0.23$	$\pm 0.02$

Table 11. Test accuracy (%) with three different annotators (Annotator1: Pairflip 45%, Annotator2: Symmetric 20%, Annotator3: Symmetric 50%) representing different noise types and noise levels on CIFAR-10, Fashion-MNIST and MNIST datasets.

adjacent categories after permutation were swapped based on a preset ratio. Asymmetric noise is a block matrix transformation, where a portion of original labels are retained and the remainder is uniformly reassigned to closest four categories.

In Figure 19 we demonstrate annotators' confusion using our algorithm on the curated MNIST dataset that showcases different image styles of Original, Thin and Thick. The strength of the regularizer,  $\lambda=0.01$ , is increased by the multiplicative scalar  $m=2$  every epoch. Figures 20, 21 and 22 highlights the original and predicted confusion of annotator 1, annotator 2 and annotator 3 using our approach with the regularizer and the non-regularized approach (that is, when  $\lambda=0$ ).

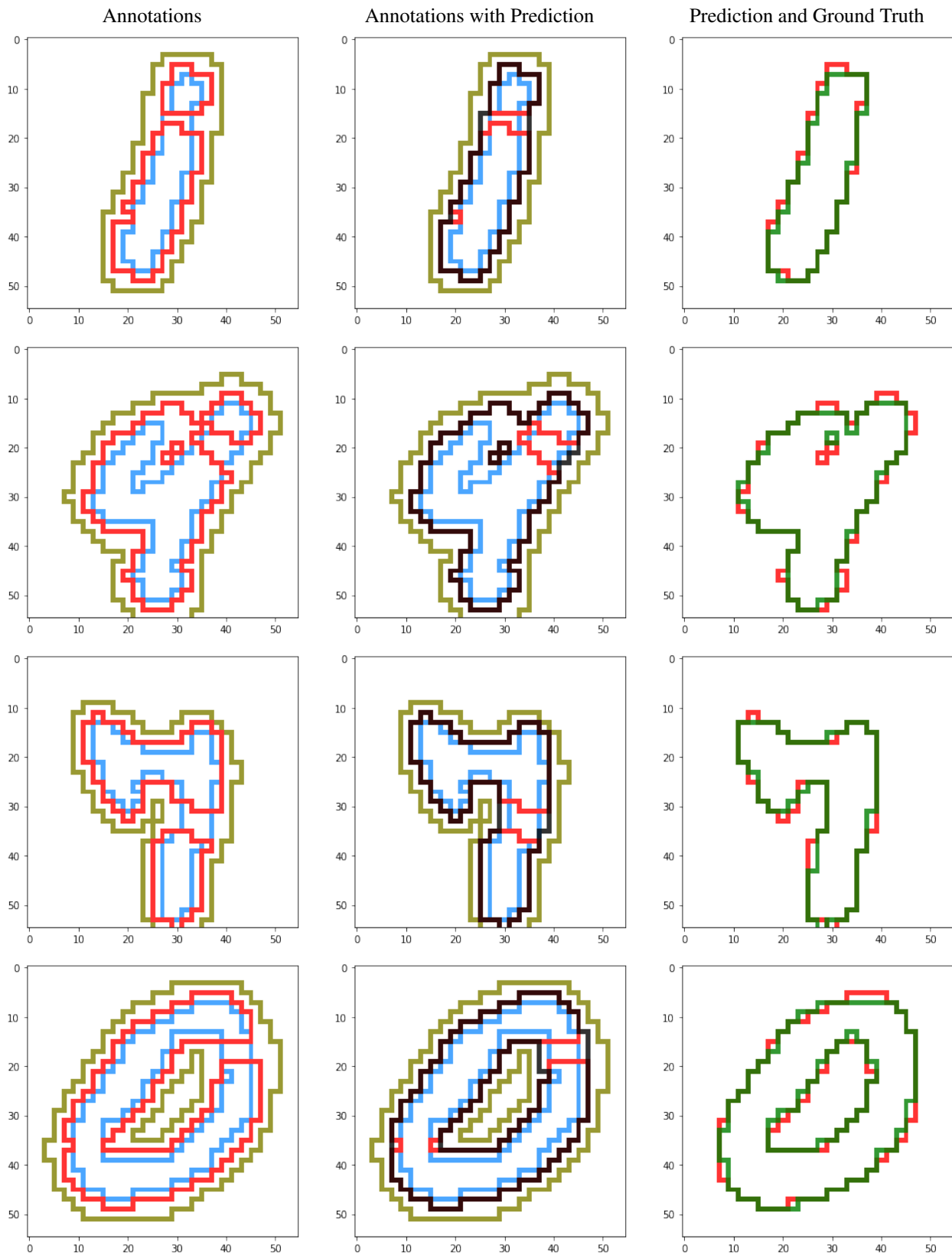


Figure 11. Visualization of segmentation results along with annotators (MNIST): left: red for fractured, dodgerblue for thin and olive for thick; middle: same colors for annotators and black for prediction; right: red for true label and green for prediction.

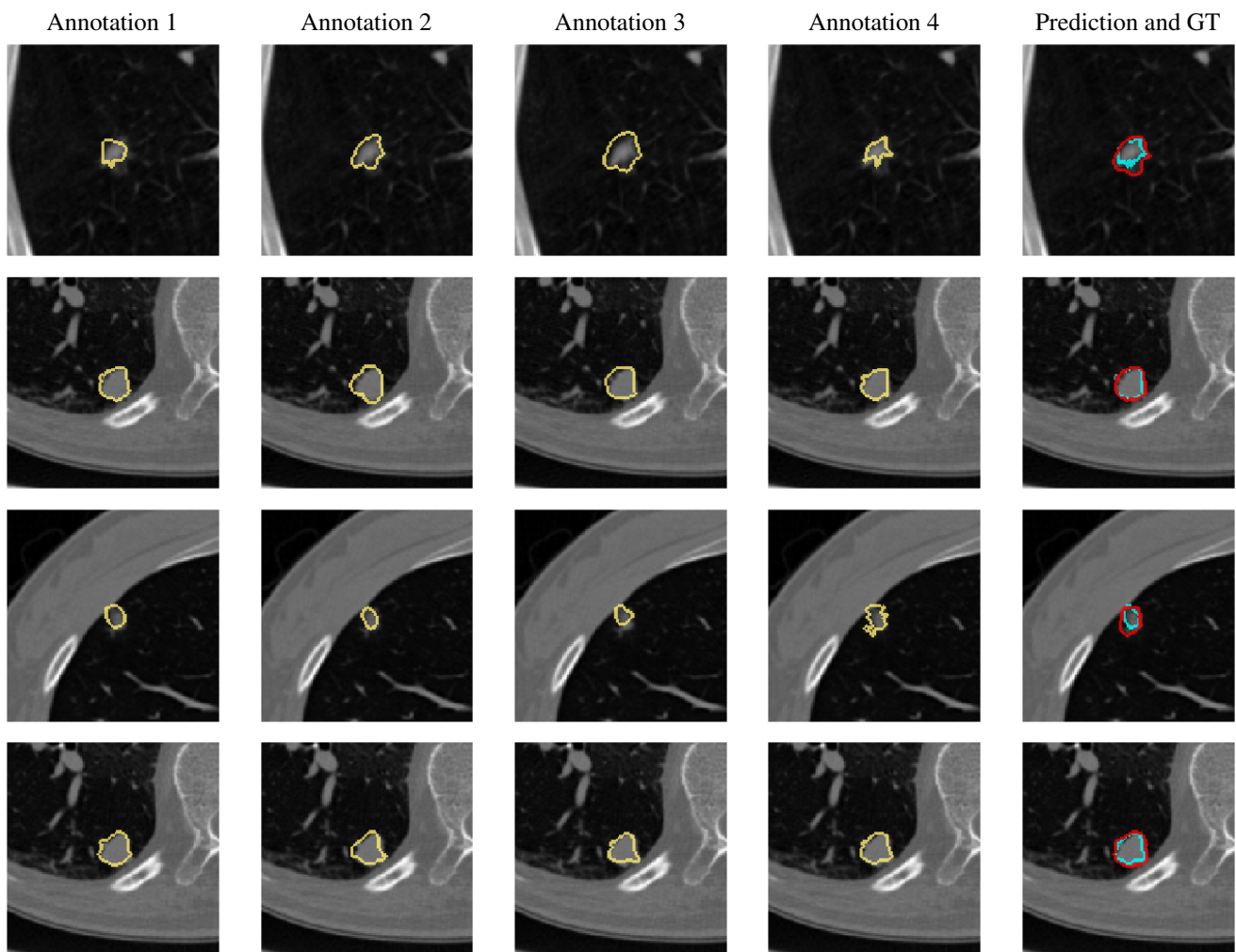


Figure 12. Visualization of all annotations and segmentation results for LIDC dataset: in the last column, prediction is in the red and true label (maj) in skyblue.



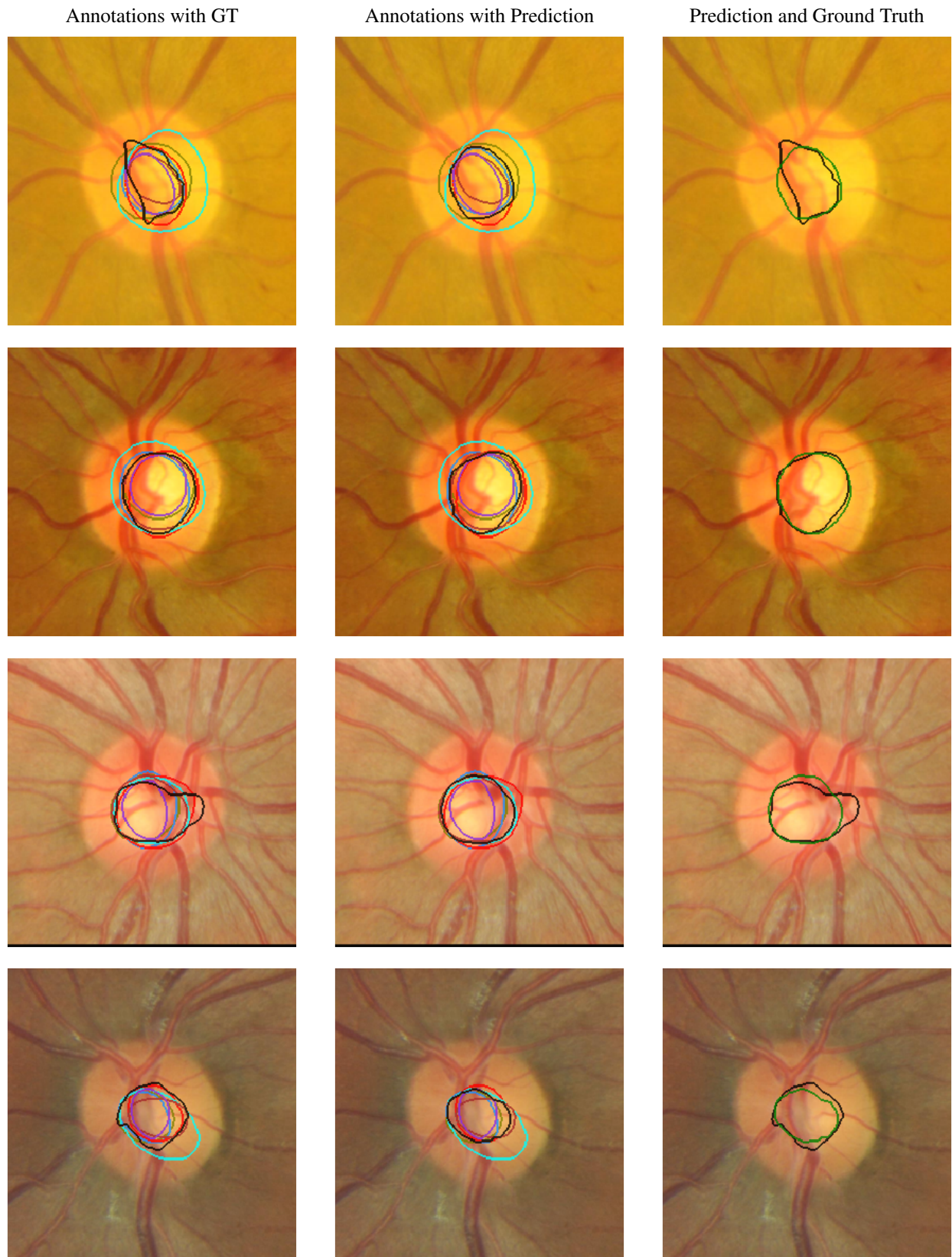


Figure 13. Visualization of segmentation results along with annotators (RIGA Optical Cup): left: all annotations and prediction (in black); middle: all annotations and true label (in black); right: prediction (in black) and true label (in green).

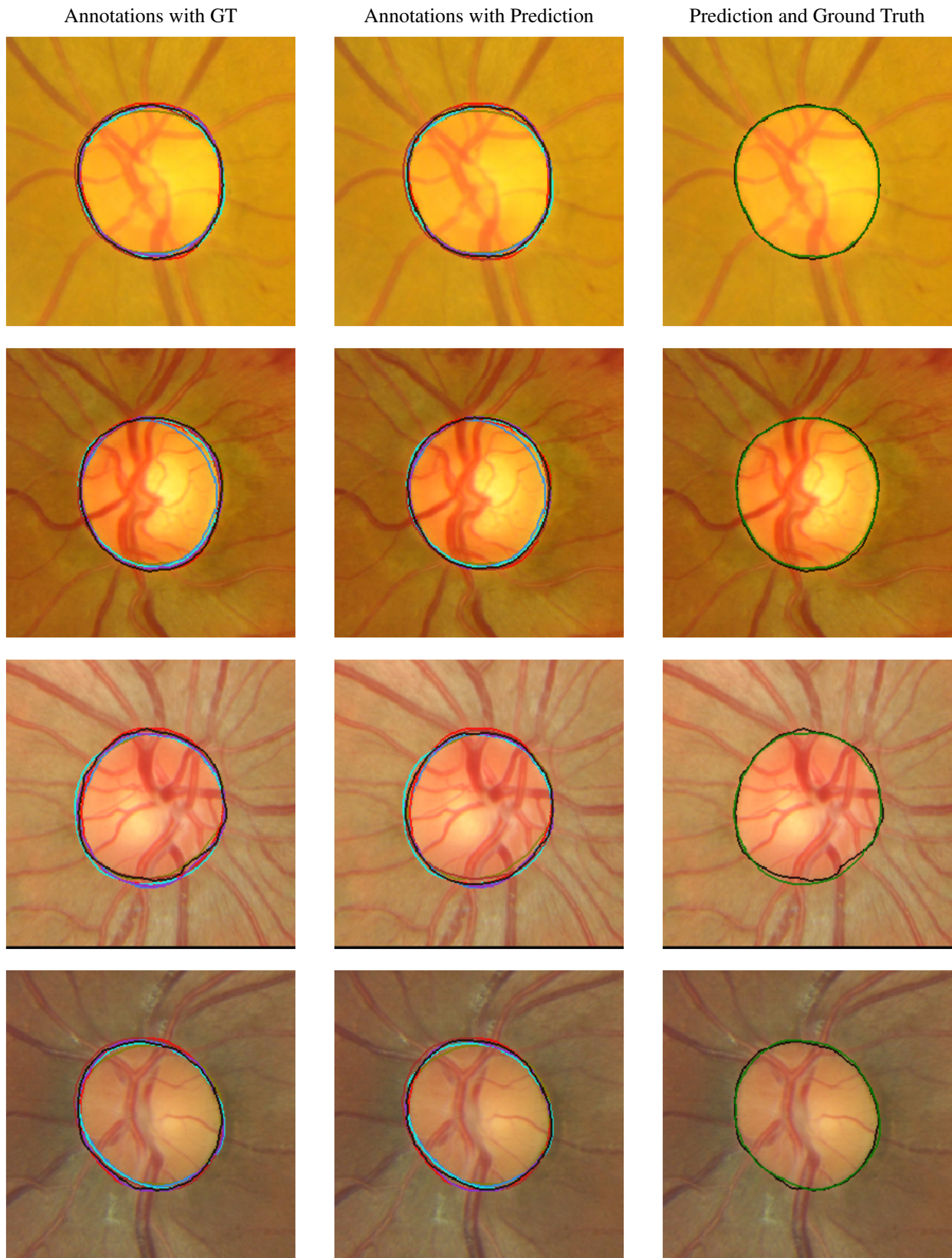


Figure 14. Visualization of segmentation results along with annotators (RIGA Optical Disc): left: all annotations and prediction (in black); middle: all annotations and true label (in black); right: prediction (in black) and true label (in green).

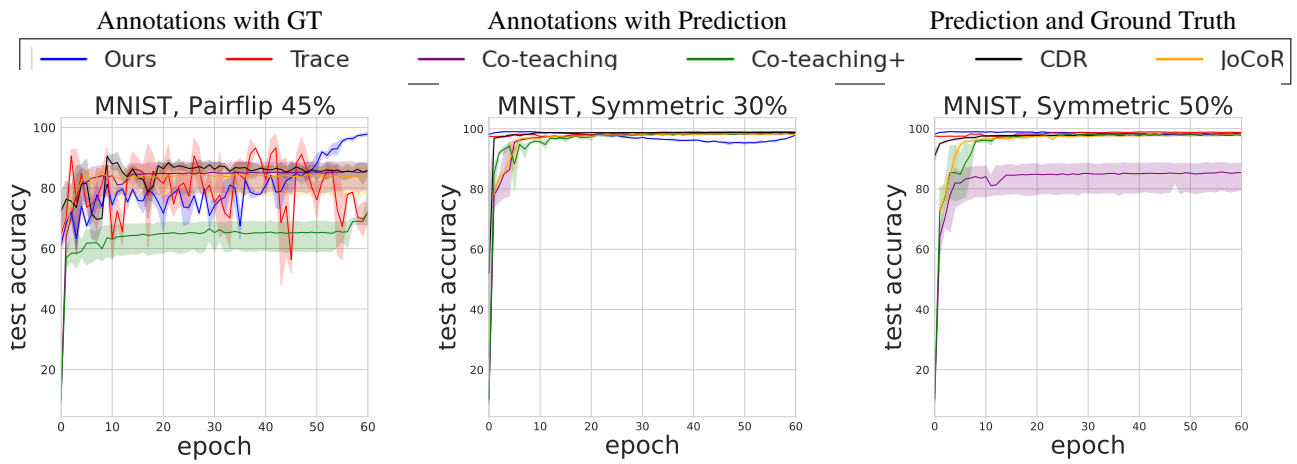


Figure 15. Test accuracy (%) vs. number of epochs on MNIST.

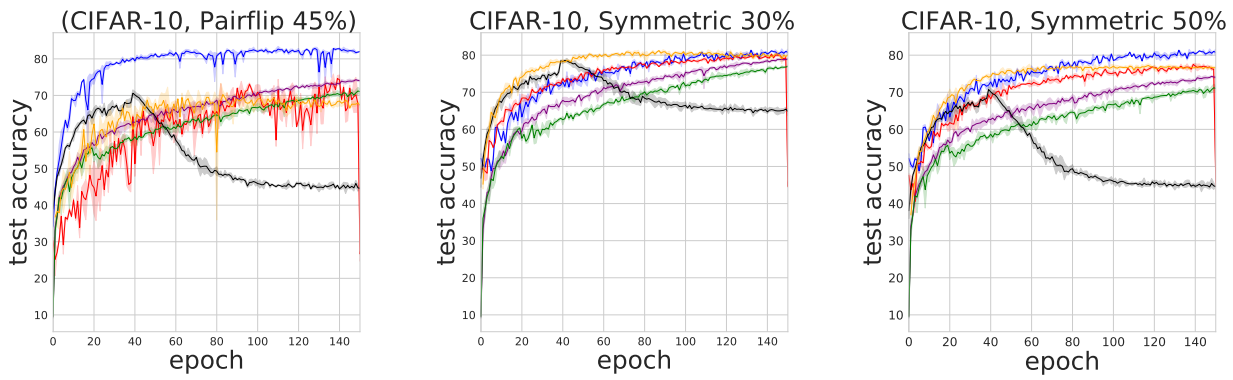


Figure 16. Test accuracy (%) vs. epochs on CIFAR-10.

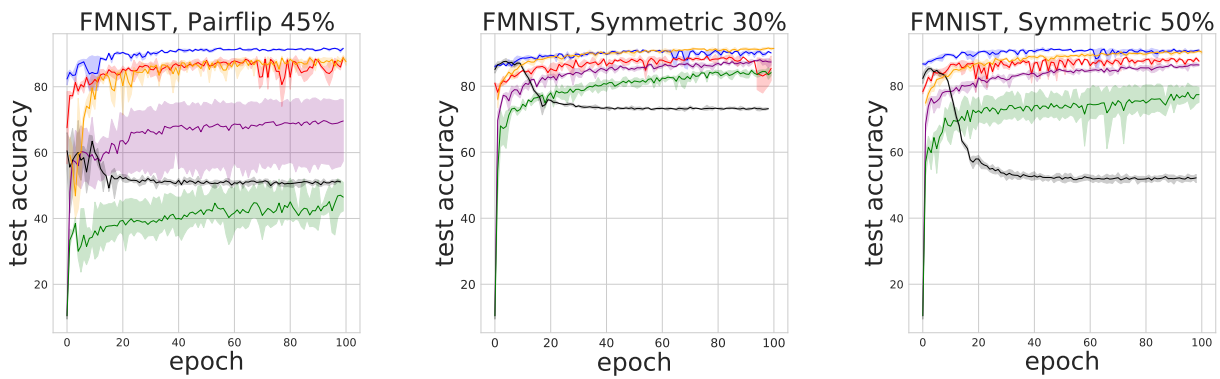
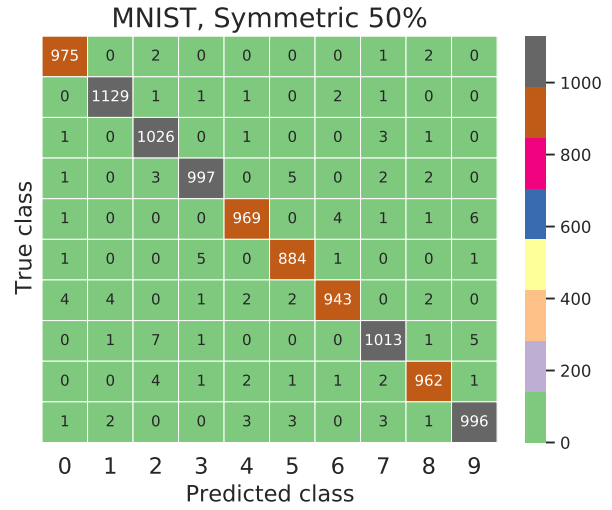
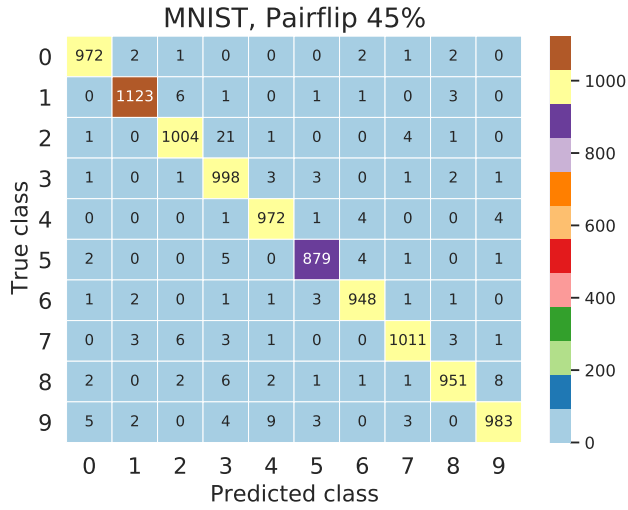
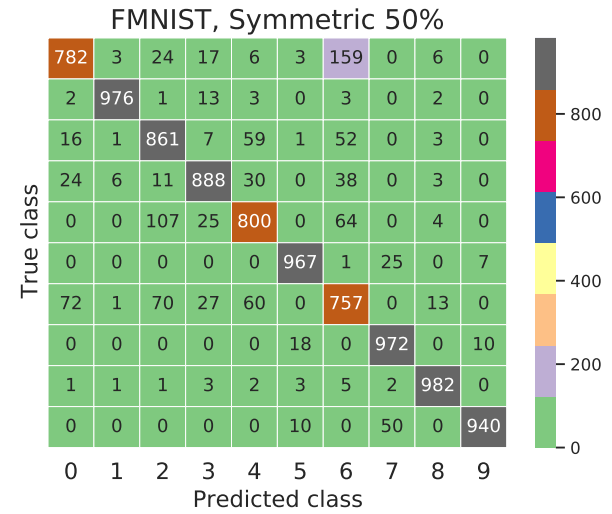
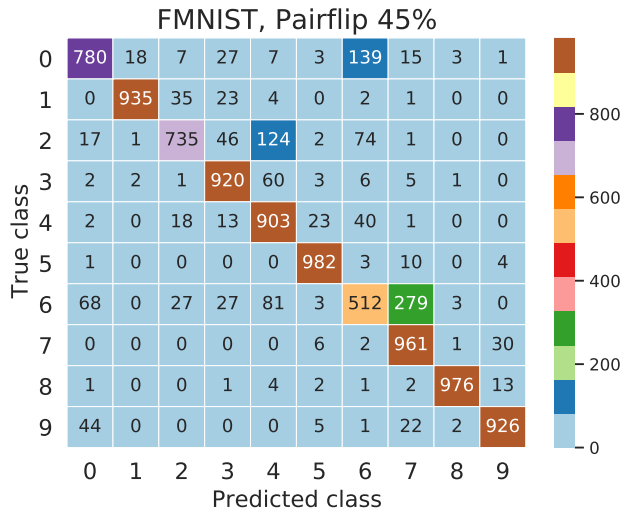


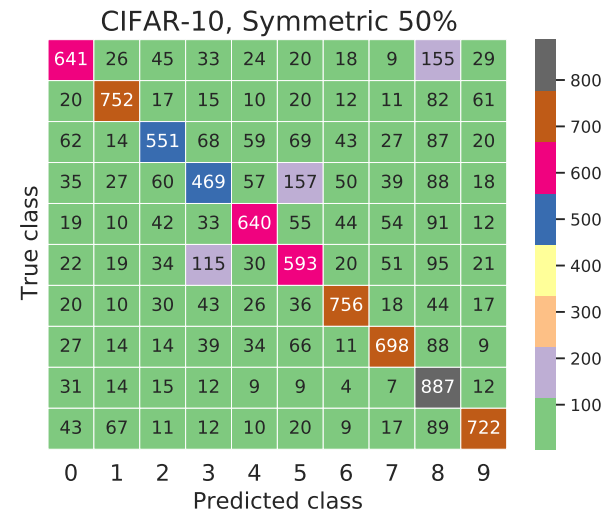
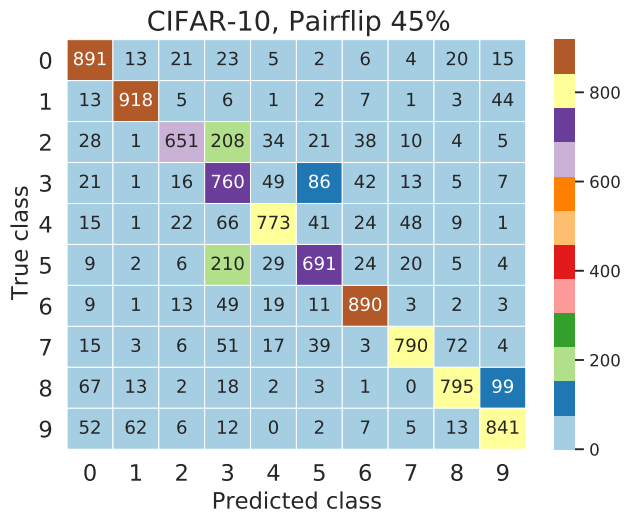
Figure 17. Test accuracy (%) vs. epochs on Fashion-MNIST.



(a)



(b)



(c)

Figure 18. Confusion matrices of true class and predicted class for our algorithm for CIFAR-10, MNIST and Fashion-MNIST datasets.

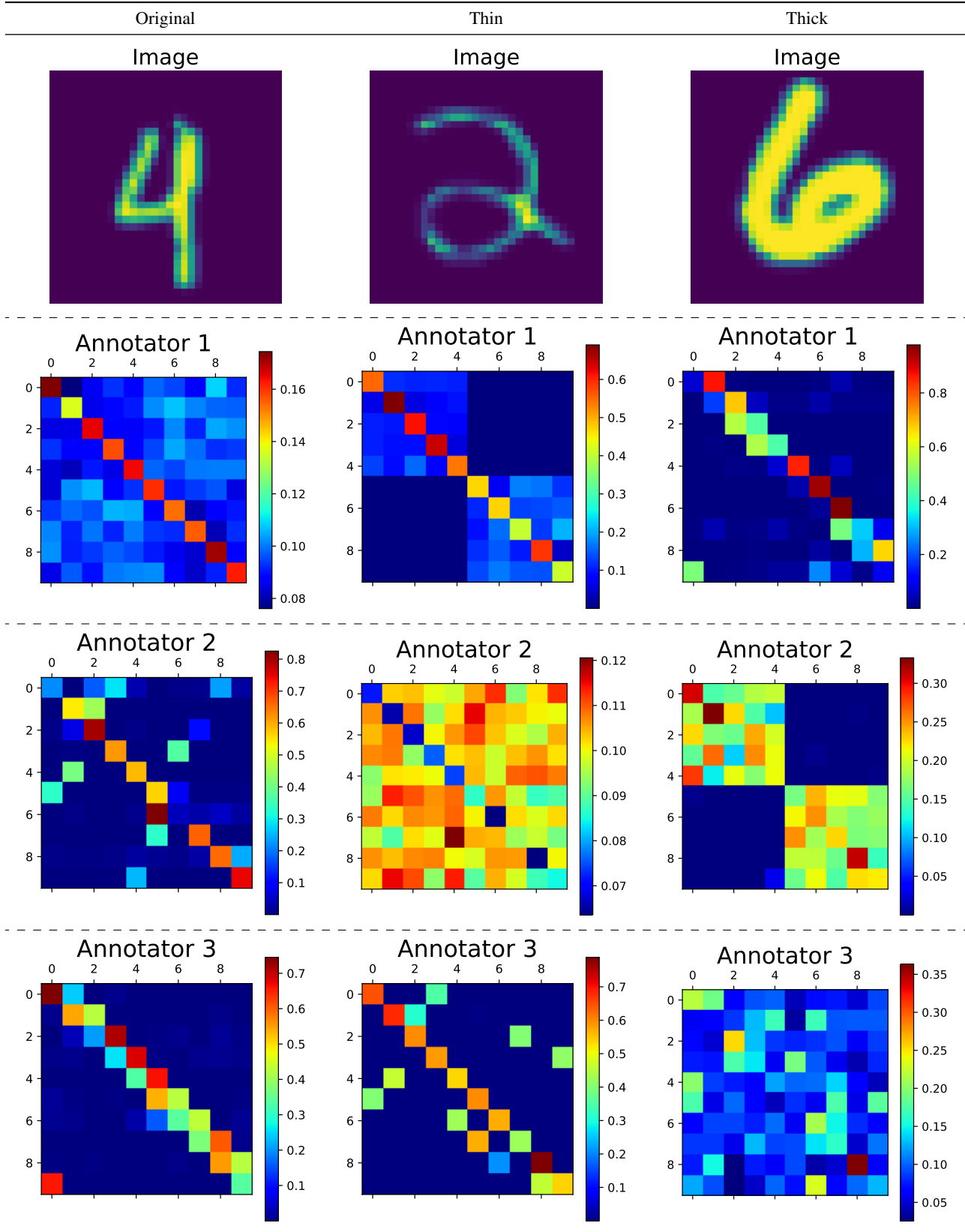


Figure 19. Learned Annotators' confusion for different image styles using our approach with the regularizer ( $\lambda=0.01$ ,  $m=2$ ) on MNIST dataset.

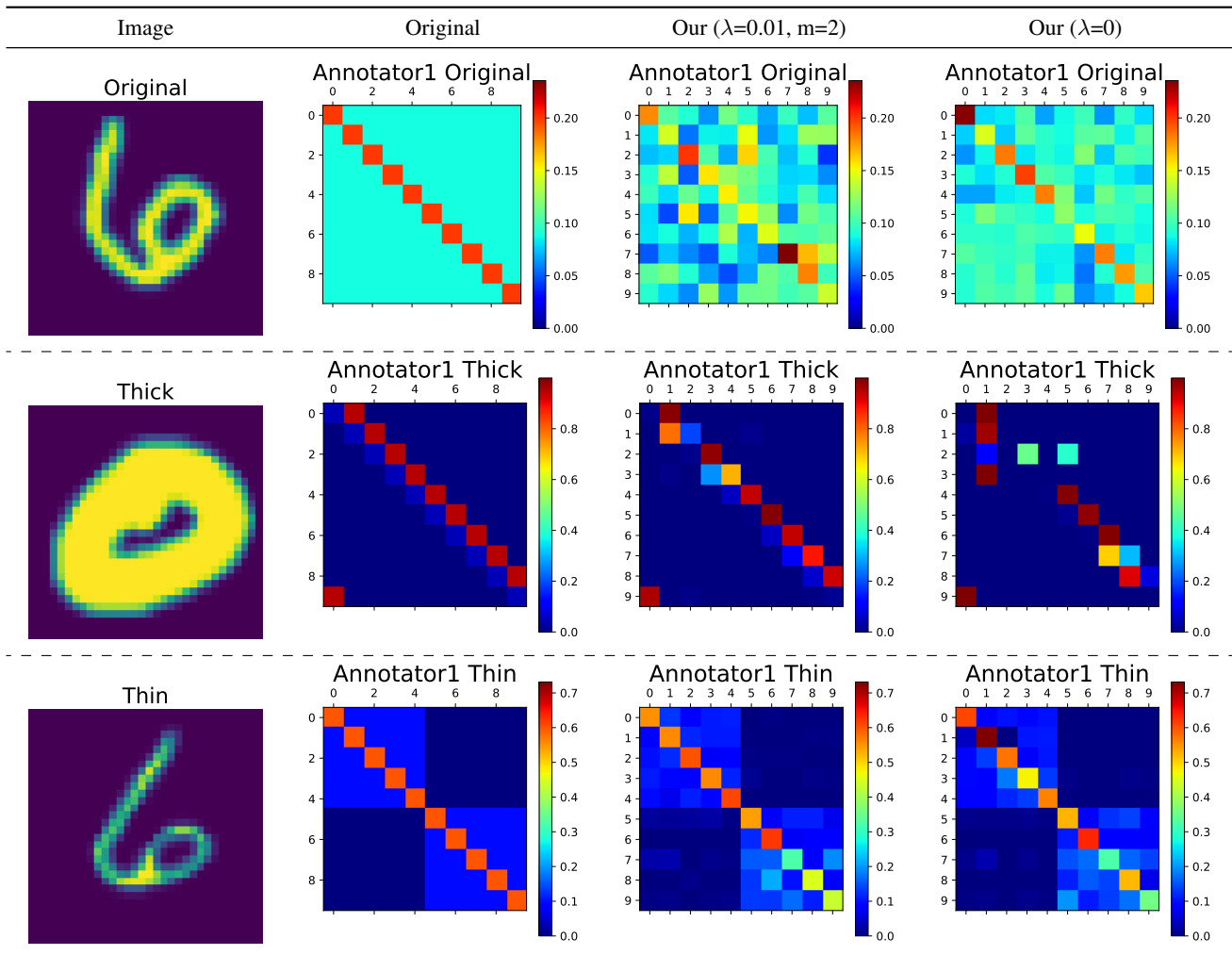


Figure 20. Original and Predicted confusion for Annotator 1 using different models: our approach with regularizer ( $\lambda = 0.01, m=2$ ) and without it ( $\lambda = 0$ ) on *MNIST* dataset.

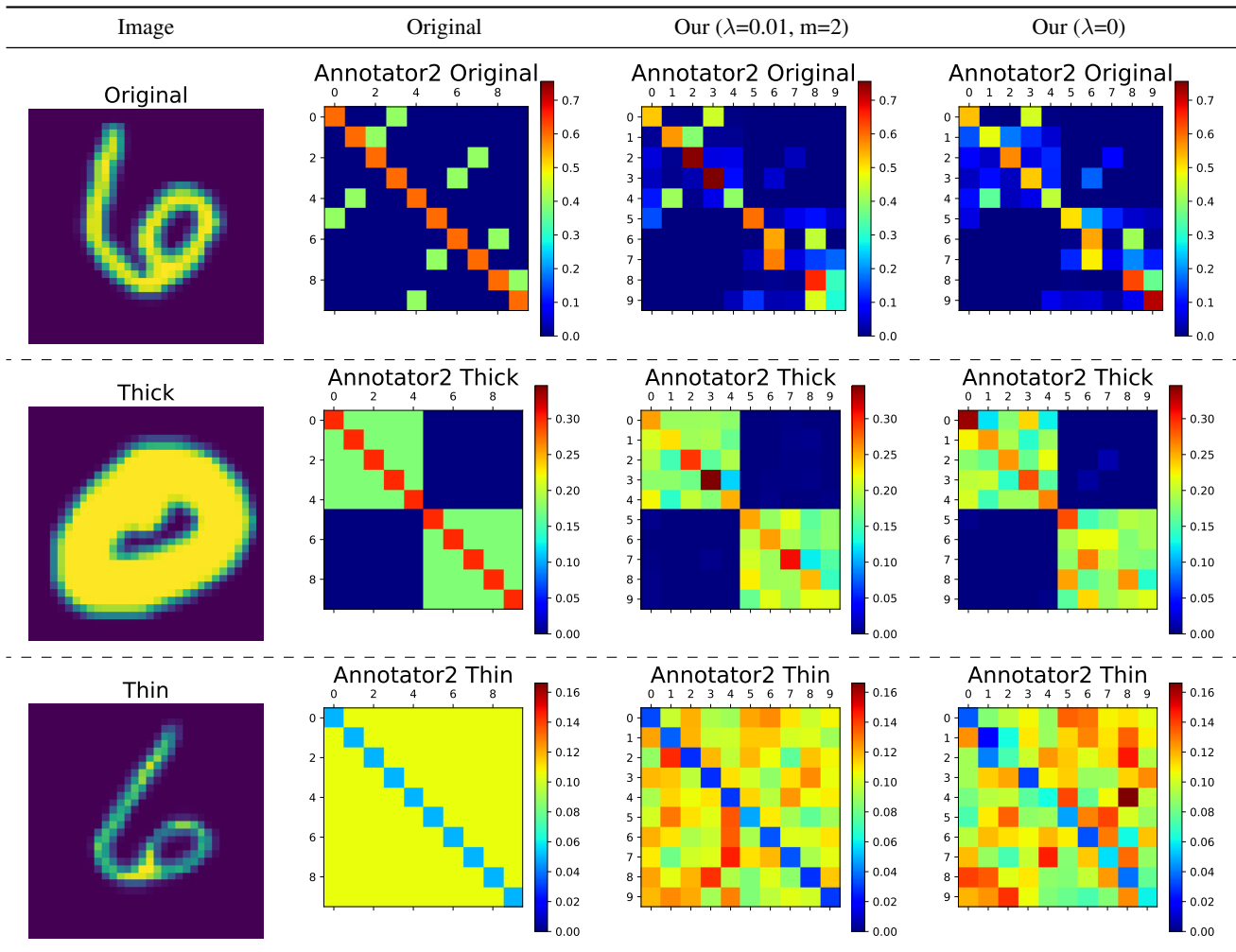


Figure 21. Original and Predicted confusion for Annotator 2 using different models: our approach with regularizer ( $\lambda = 0.01, m=2$ ) and without it ( $\lambda = 0$ ) on MNIST dataset.

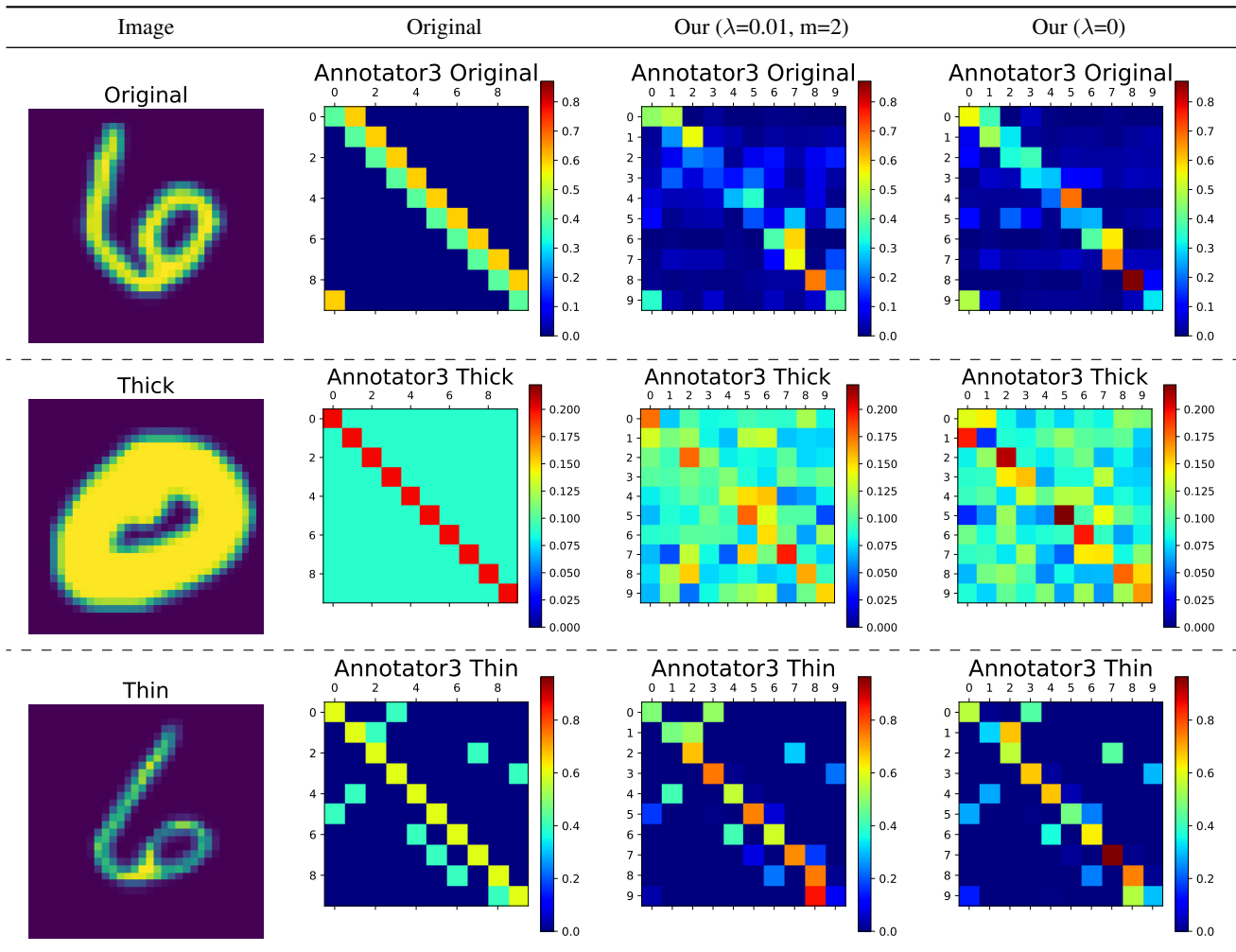


Figure 22. Original and Predicted confusion for Annotator 3 using different models: our approach with regularizer ( $\lambda = 0.01, m=2$ ) and without it ( $\lambda = 0$ ) on MNIST dataset.